Coordinated protein modules define DNA damage responses to carboplatin at single cell resolution in human ovarian carcinoma models

Jacob S. Bedia,[1] Ying-Wen Huang,[1] Antonio Delgado Gonzalez,[1] Veronica D. Gonzalez,[2] Ionut-Gabriel Funingana,[3,4,5] Zainab Rahil,[2] Alyssa Mike,[1] Alexis Lowber,[1] Maria Vias,[4] Alan Ashworth,[6,#] James D. Brenton,[4,5,#] Wendy J. Fantl, [1,7,8, #, *]

[1]Department of Urology, Stanford University School of Medicine, Stanford, CA 94305, USA.
[2]Baxter Laboratory for Stem Cell Biology, Department of Microbiology & Immunology, Stanford University School of Medicine, Stanford, CA 94305, USA.
[3]Department of Oncology, University of Cambridge, Cambridgeshire, UK.
[4]Cancer Research UK Cambridge Institute, University of Cambridge, Cambridge, Cambridgeshire, CB2 0RE, UK.
[5]Department of Oncology, Addenbrooke's Hospital, Cambridge University Hospitals, NHS Foundation Trust, Cambridge, UK.
[6]Helen Diller Family Comprehensive Cancer Center, University of California, San Francisco, 1450 Third Street, San Francisco, CA 94158, USA.
[7]Stanford Comprehensive Cancer Institute.
[8]Department of Obstetrics and Gynecology, Stanford University School of Medicine, Stanford, CA 94305, USA.

#Co-senior authors
*Correspondence: wjfantl@stanford.edu

Abstract

Tubo-ovarian high-grade serous carcinoma (HGSC) is the most lethal gynecological malignancy and frequently responds to platinum-based chemotherapy because of common genetic and somatic impairment of DNA damage repair (DDR) pathways. The mechanisms of clinical platinum resistance are diverse and poorly molecularly defined. Consequently, there are no biomarkers or medicines that improve patient outcomes.

Herein we use single cell mass cytometry (CyTOF) to systematically evaluate the phosphorylation and abundance of proteins known to participate in the DNA damage response (DDR). Single cell analyses of highly characterized HGSC cell lines that phenocopy human patients show that cells with comparable levels of intranuclear platinum, a proxy for carboplatin uptake, undergo different cell fates. Unsupervised analyses revealed a continuum of DDR responses. Decompositional methods were used to identify eight distinct protein modules of carboplatin resistance and sensitivity at single cell resolution. CyTOF profiling of primary and secondary platinum-resistance patient models shows that a complex DDR sensitivity module is strongly associated with response, suggesting it as a potential tool to clinically characterize complex drug resistance phenotypes.

Introduction

Cytotoxic chemotherapy remains a critically important treatment for cancer patients worldwide and is effective against rapidly dividing tumor cells in which the DNA damage response (DDR) is deregulated from cell cycle control [1-3]. However, durable patient outcomes are rare, even in individuals with enhanced innate sensitivity. This is due to acquisition and selection of complex cellular traits that result in therapeutic resistance [4,5]. The standard of care for women with tubo-ovarian high grade serous carcinoma (HGSC) remains carboplatin-based chemotherapy either following surgery or in a neoadjuvant setting [6-11]. Most patients (~ 60%) initially respond because of frequent impairment of DDR pathways but almost all will develop fatal platinum-resistant recurrent disease [12,13]. The exact mechanisms behind clinical platinum resistance are not well understood and consequently, there are no effective medicines specifically designed to target carboplatin resistance.

Although multiple potential resistance mechanisms have been described, including genomic alterations, enhanced DNA repair capabilities and increased drug transporter activity, they have shown limited clinical impact [9,14-16]. However, the importance of genetic reversion as a mechanism of resistance is strongly supported from clinical studies in patients with *BRCA1* and *BRCA2* mutations. These studies have demonstrated that tumors can acquire secondary somatic mutations that restore the function of homologous recombination (HR) proteins, thereby contributing to resistance both to carboplatin and poly (ADP-ribose) polymerase inhibitors (PARPi) [17-21]. Although HGSC tumors are primarily driven by DNA structural variants, especially copy number alterations (CNA) [22] there is little evidence for new selection of commonly occurring oncogenic CNAs [23].

42 Additionally, methylation, gene expression integrated with other omics data reported by
43 the Ovarian Cancer Genome Atlas (TCG) has highlighted the complexity of resistance
44 without identifying any specific therapeutic targets [24]. Single cell RNA expression studies
45 show progressive stepwise adaptation toward resistance in response to PARPi treatment
46 in ovarian cancer models. These trajectories are potentiated by epithelial to mesenchymal
47 transition states and maintained by diverse reprogramming of metabolic and stress
48 phenotypes [25]. Together these studies suggest that HGSC tumors are susceptible to a
49 broad evolutionary space to escape carboplatin and PARPi therapy.

50 Although the potential upstream genetic, epigenetic and transcriptomic effects are
51 highly diverse, they necessarily must converge on protein function within the DDR
52 network. Critically, the DDR is regulated by protein expression levels and phosphorylation
53 states [26-30]. Based on the reported heterogeneity of resistance phenotypes and possible
54 DDR responses, we hypothesized that: i) single cell proteomic analysis is required to
55 identify diverse DDR protein networks indicative of sensitivity or resistance to carboplatin
56 and ii) comparable levels of carboplatin uptake by individual cells will result in different
57 DDRs. To address our hypotheses we applied mass cytometry, known as
58 CyTOF/Cytometry by Time-Of-Flight to measure the DDR in HGSC tumor cells. CyTOF
59 is a single cell proteomic technology that can measure up to 60 parameters per cell using
60 a panel of antibodies tagged with heavy metal-chelating polymers [31-33]. We assembled a
61 CyTOF antibody panel to simultaneously measure the DDR, cell cycle phase and
62 intracellular signaling with measurements of intracellular platinum in response to
63 carboplatin alone or in combination with a PARPi. The atomic mass of platinum falls within
64 the measurable mass range of CyTOF. Critically, our study used HGSC model systems

that more closely represent primary tumors than previous models. Unsupervised analysis of millions of single cells discovered DDR protein modules recruited by cells in specific states after treatment.

Results

Validating a CyTOF antibody panel to measure the DDR and cell cycle

We designed a CyTOF antibody panel to measure the DNA damage response in individual cells throughout all cell cycle phases **(Fig. 1B, Supp. Table S1)**. Thirty five antibodies were validated for: DNA damage detection, non-homologous end joining (NHEJ) and homologous recombination (HR) repair processes, cell cycle phases, cell cycle checkpoint activation, cell cycle arrest and phosphorylated (activated) intracellular signaling pathways [34] **(Methods)**. Measurements also included a live-dead cell discriminator (either cisplatin or rhodium-103 [^{103}Rh]) and a marker for apoptosis (cleaved (c)PARP) [35,36]. All cell cycle phases were identified by gating with pRb(S807/811), IdU (demarcates cells in S-phase), cyclin E, cyclin B1, and pHH3(S28) [37] **(Supp. Fig. 1)**. In a pilot study of HeLa cells treated with a variety of genotoxic agents overall, we observed expected DDRs that validated our panel. However, visualization of the single cell data with UMAPs revealed a previously unrecognized level of DDR complexity. Some DDRs were specific to cells within a particular cell cycle phase. In other cases, cells in the same cell cycle phase showed varying responses to the different agents used but also to a given specific agent **(Supp. Text and Supp. Figs. 2 and 3)**.

87 **Modelling carboplatin resistance in clinically relevant HGSC cell lines**

88 In a previous CyTOF study we characterized HGSC tumor cell suspensions
89 disaggregated from freshly resected advanced-stage tumors, along with 13 molecularly
90 characterized HGSC cell lines [38-40]. Our data revealed that the HGSC cell lines reflected
91 specific tumor cell phenotypes identified from the primary HGSC tumors. Notably, the
92 TYK-nu cell line phenocopied poor-prognosis vimentin-expressing cells comprised of
93 both carboplatin-resistant and responsive subpopulations [38,39]. We therefore selected the
94 TYK-nu cell line as well as the UWB.289-BRCA1-null cell line derived from a highly
95 chemo-resistant HGSC tumor and its BRCA1-expressing counterpart to study the DDR
96 response to carboplatin over time. We validated our results in three spontaneously
97 immortalized HGSC cell lines (Cambridge Institute Ovarian (CIOV)1, CIOV2 and CIOV3)
98 that retained the key characteristics of their original tumors and represented distinct states
99 of platinum resistance [41] **(Fig. 1A)**.

100 The TYK-nu cell line was generated from a xenograft of a primary patient derived
101 ovarian tumor and closely phenocopies the poor prognosis HGSC cell populations
102 identified in newly diagnosed primary tumors [39], [42] **(Supp. Table 2)**. Both clinical and
103 preclinical studies showed that combining PARP inhibitors with carboplatin-based
104 chemotherapy significantly improved progression-free survival and efficacy [43-45].
105 Specifically, preclinical studies demonstrated that carboplatin's effectiveness was
106 increased by inhibiting PARP's enzyme activity and enhancing its DNA-trapping ability
107 [44,45]. We therefore designed CyTOF experiments to analyze DDRs in TYK-nu cells treated
108 with carboplatin alone or in combination with PARPi over time. Since the DDR may be
109 strongly altered by PARP DNA trapping activity, we chose to use talazoparib, as one of

110 the most potent PARP trapping agents [46-48]. Cells were exposed to either carboplatin
111 alone (8μM), carboplatin (8μM) plus talazoparib (100nM), or talazoparib alone (100nM)
112 for 24, 48, 72, and 96h [9,11]. Optimal drug concentrations were selected from dose
113 response curves **(Supp. Fig. 4** and **Methods**). At each timepoint cells were incubated
114 with ^{103}Rh (a live-dead marker), barcoded, combined, stained with the antibody panel and
115 processed for CyTOF **(Methods)** [34]. Gating for live cells (negative for ^{103}Rh), generated
116 a CyTOF dataset of 721,579 cells for downstream analysis **(Supp. Table 3)**.

117

118 **Cell cycle responses to carboplatin induce S-phase**

119 Each cell cycle phase was manually gated from the viable (^{103}Rh- c-PARP-) TYK-
120 nu cell population **(Fig. 2A and Methods)**. Under all conditions, the proportion of cells in
121 G1 was < 1%, due to the abrogated G1 checkpoint caused by *TP53* mutation [49]. All three
122 treatments promoted a dramatic and maximal increase in the proportion of cells that
123 arrested in S-phase, ~80% at 24 and 48hr, consistent with a major DDR **(Supp. Table 3)**.
124 At 72hr and 96hr, a proportion of cells had transitioned into G2, but a significant proportion
125 remained in S-phase, which was most marked after carboplatin mono-treatment. Cells
126 spent minimal time in M-phase. Although we could not determine whether cells in G0 had
127 undergone therapy-induced senescence or quiescence, both states have been
128 associated with drug resistant phenotypes [50].

129

130 **Quantifying non-apoptotic and apoptotic cell populations in response to**
131 **carboplatin**

132 CyTOF provides a unique opportunity to quantitatively measure intracellular levels
133 of platinum (^{195}Pt) [51,52]. ^{195}Pt measurements can be used as a surrogate for intracellular
134 carboplatin levels (Methods). ^{103}Rh- cells were manually gated with c-PARP to enumerate
135 apoptotic and non-apoptotic cell populations after carboplatin (C) and carboplatin +
136 talazoparib (C + T) treatments. Biaxial plots revealed that while the frequency of apoptotic
137 cells increased over exposure time (18% for carboplatin alone, 39% for carboplatin plus
138 talazoparib at 96h), a large population of cells remained non-apoptotic **(Fig. 2B)**. These
139 data are consistent with previous studies showing that TYK-nu cells are comprised of cell
140 populations with differing carboplatin sensitivities. They also show that talazoparib
141 potentiates carboplatin activity by accumulating DNA damage through the inhibition of
142 PARP-mediated DNA repair [53-55].

143

144 **Quantifying nuclear uptake of carboplatin**

145 The 2D biaxial plots indicated that a proportion of apoptotic and non-apoptotic
146 populations had comparable levels of carboplatin **(Fig. 2B)**. Box and whisker of individual
147 cell concentrations for ^{195}Pt confirmed increased carboplatin uptake over time but also
148 revealed a previously unrecognized variability in intracellular ^{195}Pt levels **(Fig. 2C)**.
149 Although median uptake levels were greater for apoptotic cells, a large proportion of non-
150 apoptotic cells within the interquartile range had the same level of carboplatin (69–89%)
151 at each time point **(Fig. 2C)**. Additionally, some cells survived despite having extremely
152 high levels of ^{195}Pt uptake.

153 Measurements of cellular carboplatin include adduct formation between proteins
154 and DNA [56]. However, the carboplatin-mediated DDR necessarily depends on nuclear

155 uptake and the formation of stable DNA adducts. We therefore developed a new CyTOF
156 protocol to measure carboplatin levels in individual intact nuclei isolated from TYK-nu
157 cells **(Supp. Fig. 5** and **Methods)**. Nuclear uptake of carboplatin increased over time but
158 at lower levels compared with cellular uptake **(Fig. 2C)**. The fold change of carboplatin
159 uptake between cells and nuclei was equivalent for apoptotic and non-apoptotic cells at
160 each time point, showing that alterations in nuclear import/export of carboplatin were not
161 the main determinants of apoptotic cell fate **(Fig. 2D)**. As seen for total cellular uptake,
162 the median carboplatin uptake was greater in the nuclei of apoptotic versus non-apoptotic
163 cells. However, we also noted that significant numbers of nuclei from apoptotic and non-
164 apoptotic cells had the same level of ^{195}Pt (65–100%) at each timepoint. The data
165 demonstrate that drug influx and efflux pumps play only a partial role in resistance.
166

167 **Mapping the DDR trajectory in single cells**

168 These pharmacodynamic and pharmacokinetic data led us to hypothesize that cell
169 populations with similar carboplatin levels, but different fates must have distinct DDRs.
170 We therefore generated a pipeline to analyze DDR dynamics temporally and in an
171 unbiased manner independent of treatment, cell cycle and cell fate **(Fig.3)**. We first
172 computed a UMAP embedding of the TYK-nu single cell data from all timepoints and
173 treatments using 29 DDR, cell cycle checkpoint and intracellular signaling proteins **(Fig.
174 4A, Supp. Fig. 6)**. The UMAP embedding revealed a predominant continuum of cells with
175 only three discernible cell populations. In contrast to UMAPs generated with phenotypic
176 markers where discrete cell populations are easily visualized (e., g T cells, B cells), this
177 UMAP was generated exclusively with intracellular functional markers (phospho-states,

178 protein levels) revealing a continuum of many subtle and different DDR functional states.
179 To identify cell subpopulations within the UMAP, we applied Leiden clustering to group
180 cells into small neighborhoods based on their DDRs **(Fig. 4A)**. These clusters were
181 visualized with different colors and each cluster's centroid was labelled on the UMAP [57].
182 Next, we used partition-based graph abstraction (PAGA) to map the relationships
183 between these Leiden clusters. In the PAGA plot, each node represents a Leiden cluster,
184 and the edges between nodes indicate the degree of connectivity between clusters. [58].
185 To align the PAGA graphs with the UMAP, the PAGA nodes were positioned at the cluster
186 centroids **(Fig. 4A-E)**. Each cluster in the PAGA graph was depicted by a pie chart
187 showing the proportions of cells from different conditions.

188 PAGA revealed that the mass of cells in the upper left of the UMAP were apoptotic
189 with a DDR signature that was distinct from non-apoptotic cells **(Fig. 4A)**. Most untreated
190 cells were in the lower right of the UMAP **(Fig. 4C)**. Upon treatment, as the effect of the
191 agents increased, cells had a trajectory toward the apoptotic cell state. For example,
192 when compared to cells treated with T alone, cells treated with C + T located further away
193 from the untreated DDR and closer to the apoptotic state **(Fig. 4C)**. Mapping the PAGA
194 graphs over time revealed a rough temporal progression. However, timepoints were not
195 discrete. For example, some cells that had been treated with C + T for 96hr had a
196 comparable DDR with untreated or treated cells at early time points. By contrast, some
197 cells treated for 24hr mapped closely to cells treated for 96hr and in proximity to apoptotic
198 cells **(Fig. 4D)**. These results demonstrated that cells are progressing and responding to
199 treatment at different rates. Cell cycle analysis showed that most cells were in G0 or S-

200 phase. Nevertheless, there was a clear signature of cells in M-phase on the lower
201 righthand corner of the PAGA graph **(Fig. 4E)**.
202
203 **Non-negative matrix factorization (NMF) to discover modules of co-occurring DDR**
204 **proteins**
205 The UMAP/PAGA analysis revealed clusters of cells with different DDRs. To
206 determine if specific protein modules influenced the positioning of cells along the PAGA
207 trajectories, we applied non-negative matrix factorization (NMF) **(Fig. 4F)**. This algorithm
208 simultaneously learns a set of co-occurring proteins within DDR modules and then
209 computes the activity of each module in each cell [59]. NMF computed eight DDR modules
210 and the contribution of each protein to each module was then visualized with a heatmap
211 **(Fig. 4F)**. Several proteins occupied more than one module; for example, PARP1 was
212 part of Modules 2 and 8, and PCNA was part of Modules 2 and 4 **(Fig. 4F)**. To determine
213 whether cells recruit different modules over time, these modules were overlaid on the
214 PAGA graphs **(Fig. 4G)**. Rather than being uniformly distributed throughout the PAGA
215 graphs, the overlays showed that most modules were confined to discrete populations of
216 cells over the time-course. Four modules with high activity mapped mostly to localized
217 regions of the PAGA graphs: apoptotic cells to Module 1, UT cells (endogenous DDR) to
218 Module 4 to, cells treated for longer times to Module 6 to late timepoints and mitotic cells
219 to Module 7.
220
221

222 **Quantifying DDR usage over time in single cells**

223 To further characterize module usage shown in the overlays we generated box
224 and whisker plots **(Fig. 4H)**. The plots showed that module activity changed over time at
225 different rates. Modules 2 and 8 were active in both endogenous and exogenous DDRs
226 at early timepoints and Module 4 was most active in untreated cells. Module 3 peaked
227 early after treatment with MRE11 and NBS1 consistent with their role as early sensors of
228 DNA damage. In contrast, Module 6 demonstrated the greatest change over time,
229 bridging pre-apoptotic and apoptotic cells (**Fig. 4G, H**). Furthermore, Module 6 usage was
230 largely driven by carboplatin and not by talazoparib in this study. Module 6 was comprised
231 of pH2AX, pATM, pCHK1, pp53 and pRPA, all proteins playing critical roles in HR DNA
232 double strand repair [60]. The recruitment of Module 6 at later timepoints suggested it could
233 be a pharmacodynamic marker of responsiveness to carboplatin-induced damage. The
234 key finding from the UMAP/PAGA/NMF analysis was that while most non-apoptotic cells
235 mapped together densely on the UMAP, functionally they could be distinguished by eight
236 distinct DDR protein modules.

237

238 **Responses of UWB1.289 BRCA1- and BRCA1+ cell lines to carboplatin**

239 To determine whether the carboplatin-mediated DDR modules identified in the
240 TYK-nu cell line are conserved in other HGSC cells, we performed a carboplatin treatment
241 time course and DDR-CyTOF analysis on the UWB1.289 BRCA1-/BRCA+ isogenic cell
242 line pair **(Supp. Table 1)** [61]. The UWB1.289 BRCA1- cell line was derived from an HGSC
243 tumor that recurred after primary debulking surgery and treatment with
244 carboplatin/paclitaxel, paclitaxel, topotecan, and gemcitabine with doxorubicin. It harbors

245 a clinically deleterious allele of *BRCA1* and a second loss of heterozygosity event
246 rendering it functionally null for BRCA1 protein function. The UWB1.289 BRCA1+ cell line
247 has partial restoration of BRCA1 function from stable expression of a *BRCA1* cDNA
248 construct[61]. We refer to each cell line as BRCA1- and BRCA1+ and together as UWB.
249 IC_{50} values of carboplatin were 36.7μM and 43μM at 72h for the BRCA1- and BRCA1+
250 cell lines respectively, confirming a previous report **(Supp. Fig. 7** and Methods) [62]. Pilot
251 experiments with low (54 μM) and high (180μM) doses of carboplatin showed greater
252 functional responses at the higher dose **(Supp. Fig. 8)**. We focused on the latter dose
253 and analyzed 521369 single cells.
254

255 **Cell cycle, cell fate and carboplatin uptake responses**

256 In the absence of carboplatin, UWB cells were primarily in G0 and S-phase, with
257 less than 6% in G1 due to TP53 mutations abrogating the G1 checkpoint **(Supp. Fig. 9A,**
258 **Supp. Table 4)** [49]. In response to carboplatin, the population of cells in S-phase
259 increased, with BRCA1- cells moving through S-phase more quickly than BRCA1+ cells.
260 By 48hr, 61% of BRCA- cells were in S-phase compared to 88% of BRCA1+ cells. By 72
261 hr, 42% of BRCA1- cells were still in S-phase, compared to 66% of BRCA1+ cells. This
262 reflects loss of the intra-S-phase checkpoint arrest in BRCA1- cells [63]. By 72h, 50%
263 BRCA1- cells had entered G0 compared to only 24% of BRCA1+ cells. The number of
264 apoptotic cells increased over time reaching 16% for BRCA+ cells and 15% for BRCA1-
265 cells at 72hr, **(Supp. Fig. 9B)**. Comparable intracellular levels of ^{195}Pt were detected
266 between genotypes and different fates **(Supp. Fig. 9B-C)**.
267

268 **Mapping the DDR in single BRCA1- and BRCA1+ cells**

269 Following a similar approach to our single-cell analysis of TYK-nu cells, we
270 clustered the UWB CyTOF data and generated PAGA graphs. In these graphs, clusters
271 of UWB cells with similar DDR profiles formed nodes, and connectivity between these
272 nodes was represented by edges **(Fig. 3, Methods, Fig. 4A–G and Supp. Fig. 9D and**
273 **E)**. UMAP embedding showed a continuum of cells, but with arrangements that were
274 more complex than those observed in TYK-nu cells **(Supp. Fig. 9D, Fig. 4A–E)**. To
275 understand the connectivity of subpopulations, we visualized the PAGA graph in a force-
276 directed layout after an additional Leiden clustering on the PAGA graph **(Fig. 5A)**.

277 The PAGA graph for UWB cells revealed a clear separation between both
278 untreated (UT) and cells treated for 6hr compared with their states at 24, 48 after 72hr of
279 treatment **(Fig. 5A–C, Supp. Fig. 9D)**. The overlaps between cells at different timepoints
280 observed for TYK-nu cells were mostly absent in the UWB cells. UWB cells treated with
281 carboplatin for 6hrs had a slight shift in their DDR from untreated cells but by 24hr, they
282 had switched to a distinct DDR profile. At 48 and 72hr post treatment, cells followed one
283 of two trajectories with different DDRS but both culminating in apoptosis **(Fig. 5B–D)**.
284 Diffusion pseudo-time (DPT) computed on the PAGA graph confirmed these trajectories
285 **(Fig. 5E)** [64]. When colored by BRCA1 status, the PAGA graph revealed only minimal
286 separation of cells in late treatment response populations **(Fig. 5F)**. When colored by cell
287 cycle phase, G0 and S-phase cells trended toward different regions of the PAGA graph
288 with M-phase cells separated from the main PAGA graph **(Fig. 5G and I)**. The differences
289 in the timing of DDR responses between TYK-nu and UWB cell lines highlight the need
290 to measure cell states at various stages of treatment.

291 **Time evolution of DDR in UWB cells revealed by NMF**

292 To determine changes in the DDR of UWB cells over time of carboplatin exposure,
293 we discovered eight DDR modules using NMF. The relative contribution of each protein
294 within a module was depicted with a heatmap **(Fig. 5H)**. Certain proteins that co-occurred
295 in TYK-nu DDR modules also did so in UWB modules, e.g., pH2AX, pATM, and pRPA
296 (Module 8), Myc, RAD51, PCNA, PARP1 (Module 6), Ki67, pChk2, pAurora (Module 7)
297 **(Fig. 5H)**. However, other modules differed between TYK-nu and UWB cells. For
298 example, Module 5, comprised of 13 DDR proteins was not found in TYK-nu cells.
299 Median-module activity in each Leiden cluster was then visualized on the PAGA graph
300 using colored pie charts **(Fig. 5I)**. Both TYK-nu and UWB cells that were in mitosis
301 recruited one module. However, unlike TYK-nu cells, most UWB cells exhibited
302 simultaneous usage of multiple modules. This was especially noticeable in untreated
303 cells, cells 6 and 24hr post carboplatin and cells in G0. All these cells recruited three to
304 five modules but by 48 and 72hr, with a few exceptions, module usage was reduced to
305 one or two.

306 The temporality of median module usage for individual cells was visualized on box
307 and whisker plots **(Fig. 5J)**. In untreated cells, Modules 2, 4 and 6 were the most active.
308 In response to carboplatin, Module 8, which includes pH2AX, pATM, and pRPA (found in
309 Module 6 in TYK-nu cells) had the greatest activity at 48 hr before decreasing at 72 hours.
310 In contrast, Module 5, the most complex module containing 16 proteins, had significantly
311 greater usage at 24, 48 and 72 hr. This suggests that while Module 8 may be necessary,
312 it may not be sufficient for responsiveness to carboplatin. The complexity of Module 5

313 suggests that a broader DDR protein network might be needed to promote apoptosis in
314 these highly chemotherapy-resistant cell lines.
315
316 **Further characterization of the HGSC DDR landscape in patient-derived cell lines**
317 To ascertain the generalizability of DDR modules, we performed an independent
318 experiment, characterizing the carboplatin-mediated DDR in our recently established
319 CIOV1, CIOV2, CIOV3 cell lines and TYK-nu cells as a control [41]. These cell lines were
320 spontaneously immortalized continuous lines derived directly from patient tumors. All
321 three cell lines harbored *TP53* mutations and showed varying responses to carboplatin
322 mimicking those in their parent tumors **(Fig. 7A)**. CIOV1 with a non-*BRCA1/2* homologous
323 recombination defective (HRD) phenotype was sensitive to carboplatin. CIOV2 harbored
324 *K-RAS* and *MECOM* amplifications classifying it as innate resistant while CIOV3 harbored
325 a *BRCA1* reversion mutation and was classified as acquired resistant (**Supp. Table 2**).
326 Based on their protein expression levels, the cell lines represented a wide range of HGSC
327 phenotypes reflecting the heterogeneity of primary tumors **(Fig. 6A)** [38,39]. Specifically, E-
328 cadherin and vimentin delineated cells that were epithelial, mesenchymal, or epithelial-
329 mesenchymal transitioning (EMT) **(Fig. 6A)** [39]. CIOV1 cells were classified as epithelial
330 because they predominantly expression of E-cadherin. CIOV2 cells displayed a mix of
331 epithelial and EMT phenotypes, with some cells expressing E-cadherin alone whereas
332 others co-expressed E-cadherin and vimentin. In contrast, CIOV3 cells were primarily
333 mesenchymal, with a small subset showing characteristics of EMT.
334 Cell lines were treated with carboplatin (8 μM), carboplatin (8 μM) + paclitaxel (5
335 nM), carboplatin (8 μM) + rucaparib (1.2 μM), rucaparib (1.2 μM), or DMSO (control) for

336 48hr. To mimic a clinical setting the CIOV cell lines all received the same drug doses. At
337 48 hr cells were harvested, bar-coded, combined, stained with the antibody panel and
338 processed for CyTOF producing a dataset of 7,206,826 cells for downstream analysis
339 **(Fig. 1B, Supp. Table 1** and **Methods)**.
340

341 **Cell cycle phase, cell fate, and carboplatin uptake in CIOV cell lines**

342 The cell lines showed different cell cycle phase distributions at baseline and in
343 response to treatments **(Fig. 6B)**. Carboplatin alone led to varying levels of cells in S-
344 phase. Adding paclitaxel or rucaparib to carboplatin produced varying effects on other
345 cell cycle phases. Paclitaxel increased cells in G0 for CIOV1, but in G0 and G2 for CIOV2
346 and TYK-nu. Rucaparib combined with carboplatin induced minimal effects in all cell lines.
347 With its innate resistant phenotype, CIOV2 was least affected by all treatments. Under
348 the drug treatment conditions studied, most cells survived with minimal apoptosis **(Fig.**
349 **6C)**.

350 There was considerable variability in carboplatin uptake among individual cells
351 which was not affected by adding paclitaxel or rucaparib. While the interquartile ranges
352 (IQRs) showed significant overlap between apoptotic and non-apoptotic cells in CIOV1
353 and CIOV3, there was much less overlap in CIOV2. This suggests that drug efflux
354 potentially through upregulated transporters may have a greater role in the innate
355 resistant CIOV2 cell line **(Fig. 6D)**.
356

357 **Relationship between epithelial mesenchymal phenotypes with cell cycle phase**

358 Given the emergence of drug resistance in epithelial/mesenchymal transitioning
359 cells, the relationships between epithelial/mesenchymal states, cell cycle and treatments
360 across the CIOV cell lines were determined [65]. As a proxy for epithelial/mesenchymal
361 phenotype, we computed an EMT score using levels of E-cadherin and vimentin in single
362 cells. An EMT score of 1 implies an epithelial phenotype while a score of 0 implies a
363 mesenchymal phenotype **(Fig. 6E and Methods)**. CIOV1 cells were the most epithelial
364 in all cell cycle phases, while CIOV2 cells were comprised of a mix of phenotypes. CIOV3
365 cells more closely mirrored TYK-nu cells which were previously shown to be
366 mesenchymal [39] [66]. EMT scores changed marginally in response to treatments but
367 significantly within a cell cycle phase. The cell lines trended toward an epithelial
368 phenotype in G1, and toward a mesenchymal phenotype in the other cell cycle phases,
369 a result, to the best of our knowledge, not reported previously. The drug resistance in
370 CIOV2 (innate) and CIOV3 (acquired) is consistent with the presence of cells with EMT
371 and mesenchymal phenotypes [67].

372

373 **NMF module activity associated with clinical response**

374 Given that the CIOV cell lines closely resembled their parent tumors in genetic,
375 molecular, and chemotherapy responses, we investigated if any NMF modules tracked
376 with *in vivo* and *in vitro* chemotherapy responses **(Fig. 7)**. We analyzed the CIOV1-3
377 CyTOF datasets using NMF Module 6, which had the highest activity in TYK-nu cells at
378 late exposure times to carboplatin **(Fig. 4H)**. Compared to vehicle-treated cells, Module
379 6 was most active in CIOV1 cells, minimally active in CIOV2, consistent with its innate

380 resistance, while there was intermediate activity in CIOV3. Module 6 usage was greater
381 for the combination of carboplatin with rucaparib compared with standard-of-care
382 paclitaxel for all three CIOV cell lines. By contrast, Module 5, discovered in UWB cells,
383 had minimal usage in all CIOV cell lines. These findings support the use of Module 6
384 recruitment as a potential indicator of response to chemotherapy.
385

386 **Discussion**

387 Our study of carboplatin resistance in human ovarian cancer was predicated on
388 the hypothesis that in response to carboplatin tumor cells selectively activate specific
389 DDR protein sub-networks or modules through changes in phosphorylation and
390 abundance. Activating the entire DDR network would be metabolically inefficient. To
391 understand the functional consequences of genetic, transcriptomic and epigenetic
392 changes which result in sensitivity or resistance to carboplatin, we capitalized on the
393 single cell attributes of CyTOF. to measure the carboplatin-mediated DDR. To understand
394 the different fates of cells with comparable levels of intranuclear carboplatin, we analyzed
395 the CyTOF datasets with UMAP embedding, PAGA and NMF **(Fig. 3)**. UMAPs generated
396 from intracellular DDR, cell cycle and signaling proteins revealed a continuum of cells
397 exhibiting a range from subtle to large differences in their DDR profiles **(Fig. 4)**. These
398 observations align with a recent study showing that ovarian tumor cells transition through
399 a series of transcriptomic states as they progress toward resistance to a PARPi [25].

400 Applying NMF we showed that DDR(s) in individual cells can be characterized by
401 distinct protein modules. TYK-nu cells tended to use one DDR protein module at a time,
402 regardless of conditions, such as cell cycle phase or duration of treatment. By contrast,

403 highly resistant UWB cell populations used multiple modules simultaneously. This was
404 most evident for cells that were untreated or exposed to carboplatin for 6 or 24 hr **(Fig.**
405 **5)**. It could be that after the patient received multiple rounds of chemotherapy, the cells
406 had reached a state of full resistance potentially maintained by recruitment of multiple
407 DDR protein modules. Nevertheless, in M-phase, both TYK-nu and UWB cells recruited
408 one unique module that contained Ki67 and pAurora, two proteins with established roles
409 in M-phase [68,69]. Stable reintroduction of *BRCA1* into UWB-*BRCA1*-null cells made little
410 difference to their overall module usage or resistance to carboplatin. While reversion
411 mutants of *BRCA1* and *BRCA2* confer resistance by restoring HR, in this case
412 introduction of *BRCA1* had minimal effect on a tumor cell that was likely maximally
413 resistant [17,20].

414 For TYK-nu and UWB cells, modules containing the transcription factors pNFKb,
415 pMyc and β-catenin (Module 3 in TYK-nu and Module 2 in UWB) were active at early
416 times. These transcription factors have established roles in promoting chemoresistance,
417 stemness and survival [70-72]. Modules containing pRPA, pATM, pH2AX and pCHK1 or
418 pCHK2 (Module 6 in TYK-nu and Module 8 in UWB) indicate active DNA repair and cell
419 cycle arrest [73]. In TYK-nu cells, Module 6 usage occurred at late times when cells were
420 in pre- and early apoptotic states suggesting that DNA repair efforts had failed **(Fig. 4G,**
421 **H)**. In UWB cells, recruitment of Module 8 was replaced by increased reliance at later
422 time points (24, 48 and 72 hours) on the more complex Module 5 **(Fig. 5I, J)**. This
423 suggested that a larger DDR protein module was necessary to maintain therapeutic
424 resistance consistent with the transcriptomic complexity as described [24,25].

425 To validate our findings, we interrogated our recently generated CIOV cell lines for
426 their usage of Module 6 discovered in the pre-apoptotic TYK-nu cells. The presence of
427 EMT and mesenchymal cell phenotypes in CIOV2 and CIOV3 is consistent with their
428 resistant characteristics [65]. Unexpectedly, we observed cell cycle -dependent changes in
429 the EMT score with more epithelial phenotypes for cells in G1. This suggests a
430 mechanism whereby E-cadherin, through its cell adhesive function with β-catenin may
431 regulate levels of transcriptionally active β-catenin and consequently downstream target
432 genes associated with proliferation such as *MYC* and *CYCLIN D1* [74]. In contrast, the shift
433 toward a more mesenchymal phenotype during S-phase and G2 may enable cells to over-
434 ride cell cycle checkpoint arrest and adapt to carboplatin-mediated DNA damage [65].
435 Module 6 usage was linked to clinical responsiveness to carboplatin across the three
436 CIOV cell lines. It was highest in carboplatin-sensitive tumor cells (CIOV1), lowest in
437 those with innate resistance (CIOV2) and intermediate in cells with acquired resistance
438 (CIOV3). Cells treated with carboplatin plus rucaparib showed the highest usage of
439 Module 6, while carboplatin plus paclitaxel showed the lowest. This was most marked for
440 CIOV1 perhaps because this patient had not received rucaparib during their treatment.
441 The minimal usage of the complex UWB Module 5 **(Fig. 5H)** across the CIOV cell lines
442 (data not shown) suggests recruitment of alternate protein modules. This may reflect both
443 greater complexity and plasticity required to maintain carboplatin resistance [75].
444 This study is limited by the inherent complexity of the DDR. Our CyTOF panel did
445 not provide full coverage of the DDR, thus potentially missing additional DDR modules.
446 Nevertheless, it successfully measured 36 phosphorylation states and protein levels with
447 established roles in the DDR, cell cycle and signaling [73,76,77]. While interactions with

448 immune cells and stroma within the tumor microenvironment were not explored, focusing
449 on tumor cell autonomous mechanisms is a critical first step in unravelling DDR
450 complexity linked to carboplatin resistance.

451 Many of a tumor's adaptive responses to therapy are targetable [29]. However,
452 differences in innate sensitivity to carboplatin between individuals and acquired
453 resistance make it difficult to determine which adaptive pathway(s) to target and the
454 optimal timing during a patient's treatment journey. We propose that monitoring Module
455 6 usage as a readout in drug screens of carboplatin combined with other medicines in
456 CIOVs could identify more beneficial therapeutic combinations for patients. The different
457 resistance states of CIOVs make them a valuable resource toward this endeavor.

458 Furthermore, our cell suspension CyTOF assays can be readily adapted for spatial
459 analyses allowing for broader characterization of resistance modules particularly in in vitro
460 model systems. This will refine the selection of antibody panels reading out both DDR
461 and immune responses in clinical trial samples. Our approach is generalizable to study
462 drug resistance in other types of cancer.

463

464 **Methods**

465 **Cell lines**

466 HeLa and OVCA3 (American Type Culture Collection (ATCC)) and TYK-nu (National
467 Institute of Biomedical Innovation, Japanese Collection of Research Bioresources Cell
468 Bank (JCRB)) cell lines were cultured in Dulbecco's Modified Eagle Medium (DMEM)
469 (Gibco), McCoy's 5A modified medium (Gibco) and Eagle's minimal essential medium
470 (EMEM) (ATCC) respectively supplemented with 10% heat-inactivated fetal bovine serum

471 (FBS) (Hyclone), 1% Penicillin-Streptomycin (Gibco) and 2 mM L-glutamine (Gibco).
472 UWB1.289 -/-BRCA1 and +BRCA1 cell lines (ATCC) (referred to in the main manuscript
473 a BRCA1- and BRCA1+) were cultured in 50% RPMI-1640 (Gibco) supplemented with
474 2mM L-glutamine, 25 mM sodium bicarbonate and 50% mammary epithelial growth
475 medium (MEGM) (Lonza) supplemented with 3% heat-inactivated fetal bovine serum
476 (FBS). G-418 (200 mg/mL Geneticin from Gibco) was added to the media for the
477 UWB1.289 BRCA+ cell line. JHOS2 (RIKEN BRC Cell Bank) cell line was cultured in
478 Dulbecco's Modified Eagle Medium/Nutrient Mixture F-12 (DMEM/F-12 (Ham), Gibco)
479 supplemented with 10% FBS, 0.1 mM MEM non-essential amino acids (NEAA, Gibco)
480 and 1% penicillin/streptomycin. CIOV1, 2, 3 cell lines (Brenton Lab, University of
481 Cambridge, UK) were cultured in DMEM/F-12 medium (Gibco) with 10% FBS and 1%
482 penicillin/streptomycin. Cells were split every 2–3 days and kept in a humidified cell
483 culture incubator at 37°C with an atmosphere of 95% air and 5% CO_2.

484 **Dose response curves for carboplatin, talazoparib, rucaparib and paclitaxel**

485 Carboplatin (Sigma Aldrich) was dissolved in water (13.5 mM stock solution) and
486 talazoparib (MedChem Express) was dissolved in DMSO (10 mM stock solution). Cells
487 were seeded in 96-well flat-bottomed plates (5000 TYK-nu cells per well for carboplatin
488 treatment, 2000 TYK-nu cells per well for talazoparib treatment, 2000 TYK-nu cells per
489 well for carboplatin plus talazoparib and 2000 BRCA1- and BRCA1+ cells per well for
490 carboplatin treatment). For measuring the IC_{50} values for each drug alone, serial dilutions
491 were performed. Starting concentrations were 1.6 mM for carboplatin and 10μM for
492 talazoparib. TYK-nu cells were exposed continuously to each drug in a two- or three-fold
493 serial dilution (9 or 11 points) for 24, 48, 72h or 96 h in triplicate and cell growth inhibitory

494 effects were determined using the Vybrant® MTT Cell Proliferation Assay (ThermoFisher
495 Scientific) **(Supp. Fig. 3A, B)**. We subsequently transitioned to the RealTime-Glo™ MT
496 Cell Viability Assay (Promega) which has the convenience of monitoring cell viability
497 continuously using the same sample well generating more information about drug action
498 with respect to time and dose dependence. We used this assay, according to the
499 manufacturer's recommendations, to determine the IC_{50} concentrations for carboplatin
500 and talazoparib for cells treated with the combination. Cells were exposed to three-fold
501 fixed ratio serial dilutions of a starting mixture of carboplatin (16μM) and talazoparib (3
502 μM). Luminescence was measured every 24 h until 72 h **(Supp. Fig. 3C and 3D)**. We
503 tried several pilot experiments holding the concentration of each drug constant and
504 varying the other (data not shown). However, the conditions chosen, 8μM carboplatin and
505 100nM for talazoparib were optimal for keeping enough cells viable for CyTOF assays
506 particularly at the later timepoints. Lower drug concentrations had only subtle effects on
507 cell cycle/DDR measurements for the times chosen. The RealTime-Glo™ MT Cell
508 Viability Assay was also used to determine carboplatin IC_{50} values for BRCA1- and
509 BRCA1+ cells **(Supp. Fig. 7)**. The IC_{50} values at 72 h were used to guide the carboplatin
510 concentrations chosen for experiments, 54 and 189μM.

511 **Cell line treatments**

512 HeLa cells were cultured in 10cm dishes to a confluency of ~80%. They were exposed to
513 the following DNA damaging agents: 5Gy ionizing radiation (IR) **using a Cesium 137**
514 **irradiator,** followed by a 30 min rest, 100 J/m^2 ultraviolet C (UVC) followed by a 90min
515 rest, 10μM etoposide (Sigma Aldrich) with 0.02% DMSO control for 24h or 316.7μM

516 carboplatin for 24 or 48h with H_2O as control. Cells were also treated with 100ng/mL
517 nocodazole (Sigma Aldrich), a microtubule inhibitor for 18h with 0.01% DMSO control.

518 TYK-nu cells were treated with 8μM carboplatin or 8□M carboplatin plus 100nM
519 talazoparib for 24, 48, 72 and 96h, with H_2O as control harvested at 96 h.

520 UWB.289 BRCA1- and BRCA1+ isogenic cell lines were treated with 54μM or 180μM
521 carboplatin for 6, 24, 48 and 72h with H_2O as a control for 72 hr. CIOV1, CIOV2, CIOV3,
522 and TYK-nu cells were treated with 8μM carboplatin, 8μM carboplatin + 5nM paclitaxel
523 (Sigma-Aldrich, dissolved in DMSO), 8μM carboplatin + 1.2μM rucaparib (Selleckchem,
524 dissolved in DMSO), or 1.2μM rucaparib for 48h with 0.012% DMSO control for each cell
525 lines. Treatment conditions for cell line experiment were performed in triplicate. Each time
526 after treatment, cells were incubated with 10mM iododeoxyuridine (IdU) (Sigma Aldrich)
527 and viability dyes. For HeLa cells treated with all agents, aside from carboplatin, cells
528 were treated with 25mM cisplatin (Sigma Aldrich) for 1 min as previously described [34].
529 For experiments with carboplatin, cells were treated with 1mM Cell-ID™ Intercalator-
530 103Rh (Standard BioTools) for 15 min as previously described [34]. Cells were
531 subsequently harvested, fixed with 1.6% paraformaldehyde, washed twice with CSM,
532 flash-frozen, and stored at - 80°C [34,39].

533 **Isolation of nuclei**

534 Untreated and carboplatin-treated 4–5 x 10^6 TYK-nu cells were harvested at different
535 timepoints (24, 48, 72, and 96 h). Half the cell aliquot was processed as described above.
536 The other half of the aliquot was processed for isolating nuclei. TYK-nu cells, cell pellets
537 were resuspended in 300 μL of cold lysis buffer (Tris-HCl pH 7.4 (10 mM), NaCl (10 mM),

538 $MgCl_2$ (3 mM) and Igepal CA-630 (0.025% in PBS, Millipore Sigma) and incubated on ice
539 for 10 min (time optimized from 10X Genomics protocol). The reaction was quenched with
540 1.2 mL of cold cell staining media (CSM) and suspensions of nuclei were washed twice
541 with CSM (500 x g, 10 min, 4°C). Nuclei were fixed in 1 mL 1.6% PFA in PBS for 10 min
542 at room temperature, washed twice with CSM, resuspended in CSM (~150-200 µL), snap
543 frozen in dry ice, and stored at 80°C.

544 **Confirming purity of isolated nuclei**

545 The purity of the nuclei was evaluated using an anti-histone H3 antibody (D1H2 (Standard
546 BioTools)) by CyTOF and then gating for non-apoptotic and apoptotic cells using a c-
547 PARP antibody **(Supp. Fig. 4A)**. Additionally, purity of the nuclei was determined by
548 comparing their scatter properties with those of whole cells **(Supp. Fig. 4B)** using an
549 LSR2 flow cytometer. Further confirmation of purity was confirmed by microscopy with
550 DAPI (blue) and vimentin-Ax647 (D21H3 (CST)) using a Keyence BZ-X800 microscope
551 **(Supp. Fig. 4C)**.

552 **Antibodies for CyTOF**

553 Antibodies were all conjugated in-house **(Supp. Table 1)**. In brief, antibodies in carrier-
554 free PBS were conjugated to metal-chelated polymers (MaxPAR antibody conjugation kit,
555 Standard BioTools) according to the manufacturer's protocol. Bismuth-chelated polymer
556 labeling was performed with an in house- protocol [78]. Metal-labeled antibodies were
557 diluted to 0.2–0.4 mg/mL in antibody stabilization solution (CANDOR Biosciences) and
558 stored at 4°C. Each antibody was titrated using positive and negative controls as
559 described **(Supp. Table 1)**. Antibody concentrations chosen were based on optimal
560 signal-to-noise ratio.

561 **Sample processing and antibody staining for CyTOF**

562 Frozen, fixed single-cell suspensions of cell lines were thawed at room temperature. For
563 each sample, 1 x 10^6 cells were aliquoted into cluster tubes in 96 well plates and
564 subjected to pre-permeabilization palladium barcoding [79,80]. After barcoding, cells were
565 pooled, washed, and incubated for 5 min at room temperature with FcX block (Biolegend,)
566 to block non-specific antibody binding. Cells were then incubated with the CyTOF
567 antibody panel, washed, and incubated with the $^{191/193}$Ir-intercalator at 4°C overnight.
568 Cells were resuspended in a solution of normalization beads washed and resuspended
569 before introduction into the CyTOF2 [39].

570 **Sample processing and antibody staining of isolated nuclei**

571 Fixed frozen TYK-nu nuclei were thawed at room temperature. Samples were transferred
572 into cluster tubes containing 1 mL of cold CSM and washed (600 x g, 10 min, 4 °C).
573 Samples were permeabilized in 1 mL 100% ice-cold methanol for 20 min at 4 °C, washed
574 twice with cold CSM and stained with antibodies against vimentin (D21H3 (CST)) and
575 intra-nuclear markers (Histone H3, c-PARP (F21-852 (BD)) for 1 h at room temperature
576 on a shaker. Samples were washed twice with cold CSM and incubated in 1 mL $^{191/193}$Ir
577 DNA intercalator solution (0.1 μM) in 1.6% PFA (PBS) overnight at 4 °C. TYK-nu nuclei
578 suspensions were washed once with CSM and twice with CyTOF water, prior being
579 resuspended in a solution of normalization beads and introduced into the CyTOF2.
580 Platinum was read out on the 195 channel, as it represents the most abundant stable
581 platinum isotope.

582

583 **Processing frozen nuclei for microscopy**

584 Fixed frozen TYK-nu nuclei were thawed at room temperature, transferred to FACS tubes
585 containing 1 mL of cold CSM and washed (500 x g, 10 min, 4 °C). Samples were
586 permeabilized in 100% ice-cold methanol (1 mL) for 20 min at 4 °C, washed twice with
587 cold CSM and stained with vimentin-A647antibody (5 µL in 100 µL of reaction) for 30 min
588 on ice. After addition of 2 mL CSM, samples were washed twice with CSM followed by
589 staining with DAPI (1 µg/ mL in CSM, 500 µL) for 10 min at room temperature. After two
590 washes with CSM, nuclei were resuspended in 100 µL of CSM. 10 µL of nuclei in
591 suspension were transferred onto a microscope slide, a coverslip was placed on top
592 samples were imaged using the Keyence microscope BZ-X800.

593

594 **Data analysis tools and illustration design software**

595 All data, statistical analysis, and figures were conducted with Adobe Illustrator, Microsoft
596 Excel, Microsoft PowerPoint, R 4.1.2, Python 3.7, MATLAB 2019, and GraphPad Prism
597 8. CyTOF datasets were evaluated with software available from Cytobank and
598 CellEngine. The study schematic and signaling map (Fig. 1) were created with
599 BioRender.com. Biaxial plots **(Fig. 2B)** were generated in CellEngine
600 (https://cellengine.com). Dose response curves and IC-50 values in **Supp. Fig. 3C**,
601 **Supp., Fig 4**, and **Supp. Fig. 7** were generated using GraphPad Prism 8. Supplementary
602 Figure 4A, 4B, and 5A were generated with Microsoft PowerPoint. Multiplexed Louvain
603 community detection in Fig 4C was performed using a modified script in MATLAB 2019
604 http://netwiki.amath.unc.edu/GenLouvain, https://github.com/GenLouvain/GenLouvain
605 (2011-2019). and a custom pre-processing script written in R. All other analyses and

606 figures were generated using custom R and Python scripts written in-house that are
607 publicly available. Specific package requirements for scripts are included in code.
608 Analyses in CellEngine and Cytobank were performed at cellengine.com and
609 cytobank.org, respectively. Analyses in Python and MATLAB were performed on a
610 custom-built server running Windows 10 with 256 GB RAM. All other analyses were
611 performed on a MacBook Pro with 64 GB RAM.

612 **Initial assessment of data quality and cell fate identification**

613 CyTOF FCS files were normalized and debarcoded using algorithms reported previously
614 [80,81] with access at the two links https://github.com/ParkerICI/premessa
615 https://github.com/nolanlab/bead-normalization/wiki/Normalizing-FCS-Files
616 Tailored manual gating was performed in the Cytobank or CellEngine software. Singlets
617 were gated based on ^{191}Ir/^{193}Ir DNA content and event length to exclude debris and
618 doublets. Following singlets gating, cells were gated using viability dye (^{103}Rh or cisplatin)
619 into dye positive and dye negative populations. Dye negative populations were further
620 gated based on levels of c-PARP into non-apoptotic/viable (c-PARP-) and apoptotic (c-
621 PARP+). Cisplatin was used as a viability dye in HeLa cells [35]. For experiments with
622 carboplatin treatments, ^{103}Rh was used as an alternate viability dye.

623 **Measurements of cell cycle**

624 Cell cycle distribution was measured by applying the manual gating strategy
625 described previously [37]. Viability dye negative cells were used to analyze the cell cycle
626 for each condition. Gating strategy is summarized in **Supp. Fig. 1**. To delineate cell cycle
627 phases, we first utilized IdU to identify cells in S phase, and an antibody against cyclin B1
628 to demarcate the rest of the cells in G0/G1 and G2/M phases. Antibodies against pRb

629 (S807/811) and cyclin E were applied to separate G0 and G1 phases. G2 and M phases
630 of the cell cycle were distinguished by gating with antibody against pHH3 (S28).

631 **Cell Line DDR Mutation Profiles**

632 GO analysis was performed using AmiGO2 searching Genes and Gene Products with
633 keyword DNA+Damage+Response. From organism drop down Homo sapiens was
634 selected and from Type column protein was selected. Results were downloaded as
635 txt file on April 28, 2022. Results from depmap were downloaded by searching for cell
636 lines from Cell Line Selector. Mutations were downloaded. Then script in R was used
637 to match genes identified with GO analysis to mutated genes in cell lines and results
638 were saved in **Supp. Table 2**.

639

640 **Computational analysis**

641 **Cell cycle phase pie charts**

642 Cell cycle phase pie charts were computed as the proportion of non-apoptotic cells in
643 each cell cycle phase and generated in ggplot2.

644 **Protein expression violin plots**

645 Violin plots were generated in ggplot2 using live cells (Cisplatin-negative for HeLa cells
646 in Figure 2 and Rh-103 negative for all other single cell data)

647 **Platinum uptake box and whisker plots**

648 Notched box and whisker plots were generated in ggplot2. The notches extend 1.58 * IQR
649 / sqrt(n) which gives a roughly 95% confidence interval for comparing medians [REF
650 McGill et al. (1978)]. Data were $\log_{10}$ normalized prior to visualization.

651 **Fold change nuclei isolation**

652 Median platinum levels were extracted for both non-apoptotic and apoptotic cells and
653 nuclei. The ratio of median nuclear to cellular platinum levels for both apoptotic and non-
654 apoptotic cells was used to construct the bar chart.

655 **LDA**

656 Linear discriminant analysis (LDA) was computed using the MASS package in R. A
657 training set and test set with balanced classes were generated from viable HeLa single
658 cell data. For each treatment (class), 7000 cells were randomly sampled then randomly
659 partitioned into 6300 cells for the training set and 700 cells for the test set. This resulted
660 in a training set of 31500 cells and a test set of 3500 cells. Linear discriminant functions
661 (LDFs) were fit using the MASS::lda function on the single cell DDR protein expression
662 levels for cells in the training set. Markers for cell cycle phase, apoptosis, and viability
663 were excluded. To test the quality of fit, four LDFs were used to predict treatment from
664 DDR protein levels on the test set and classification results were reported in confusion
665 matrix. The macro-F1 score was used as a summary statistic for the performance of the
666 final fit LDFs. The macro-F1 score is defined as the average F1 score over all treatments
667 and is summarized in the following equation:

668 $$\text{macro-F1} = \frac{1}{n}\sum_{\mathrm{i}=1}^{\mathrm{n}} \frac{\mathrm{TP_i}}{\mathrm{TP_i} + \frac{1}{2}(\mathrm{FP_i} + \mathrm{FN_i})}$$

669 where the value in the sum is the F1 score for treatment *i* and TP_i, FP_i, and FN_i denote
670 the number of true positives, false positives, and false negatives for group *i*, respectively.
671 The waterfall plot displaying the loadings of LDF1 was generated using ggplot2 in R.

672 **Single cell data visualization**

673 Single cell data were visualized using the scanpy package in Python [82]. To denoise the
674 data, cells with total expression (sum over all marker expression levels) higher than the
675 99.5% quantile were excluded. For normalization, we apply the approach to the standard
676 normalization pipeline in Monocle3 (https://cole-trapnell-lab.github.io/monocle3). After
677 normalization, principal component analysis (PCA) was applied to reduce the data
678 dimensionality. Based on a waterfall plot of % variance explained vs. principal component
679 (PC), the top 10 PCs with highest % variance explained were selected. Next, a nearest
680 neighbor graph was constructed on the single cell data, with k = 30 nearest neighbors.
681 Uniform Manifold Approximation and Projection (UMAP) was applied to this data with
682 default parameters and the results were visualized using ggplot2. This procedure was
683 performed separately for HeLa cells **(Supp. Fig. 2D, E, Supp. Fig 3D-G)**, TYK-nu cells
684 **(Fig. 4A)**, and UWB cells **(Supp. Fig. 9D).**

685 **Clustering, PAGA, and DPT**

686 Single cell data were clustered with the Leiden algorithm in scanpy [57]. The Leiden
687 algorithm was selected since it has been shown to identify connected communities more
688 accurately than Louvain. The role of clustering in this study is not to identify distinct cell
689 phenotypes but to define similar (often overlapping) groups of cells whose characteristics
690 (such as cell cycle phase, treatment, and cell fate) can be analyzed in the context of the
691 larger dataset. In this respect, the goal was to generate a sufficient number of clusters to
692 cover the manifold while keeping the number low enough to enable reasonable
693 visualization and downstream analyses. Clustering was performed separately for the
694 TYK-nu and UWB time course experiments. For both datasets, pre-processed as
695 described in the previous section, a nearest neighbor with k = 30 nearest neighbors was

696 constructed, and Leiden clustering with resolution = 5.0 was run. Results were visualized
697 in ggplot2. After clustering, PAGA was used to compute the connectivity between the
698 identified clusters with default parameters [58]. Edges with PAGA weights less than 0.1
699 were excluded. PAGA graphs were visualized in the R igraph package. Diffusion
700 pseudotime (DPT) **(Fig. 5E)** was computed with default parameters using the scanpy
701 package.

702 **NMF**

703 NMF was computed using the consensus NMF approach with the scikit-learn package in
704 Python [59]. To denoise the data, cells with total expression (sum over all marker expression
705 levels) higher than the 99.5% quantile were excluded. Data were then row normalized
706 and scaled to unit variance. Consensus NMF modules were then computed by computing
707 100 sets of modules using the NMF function in scikit-learn, with max_iter = 3000. K was
708 set to 30 for KNN-deviation and only modules that fall within a distance threshold of 0.1
709 were kept. Resulting modules were visualized using the gplots package in R and
710 ComplexHeatmap **(Figs 4F and 5H)**. For cell line specific NMF, eight modules were
711 computed using the above approach for each cell line separately. Box and whisker plots
712 showing module activity over time were generated in ggplot2.

713

714 **Resource availability**

715 **Lead contact**

716 Further information and requests for resources and reagents should be directed to and
717 will be fulfilled by the lead contact, Wendy J. Fantl (wjfantl@stanford.edu)

718 **Materials availability**

719 This study did not generate new unique reagents.

720

721 **Data and code availability**

722 All data reported in this paper will be shared by the lead contact upon request.

723

724 **Acknowledgements**

725 This work was supported by funding from the BRCA Foundation and the V Foundation
726 for Cancer Research; a gift from the Gray Foundation, Department of Defense
727 (W81XWH-12-1-0591), NCI (1R01CA234553, R21CA231280), the 2019 Cancer
728 Innovation Award, the 2021 Cancer Innovation award both supported by the Stanford
729 Cancer Institute, an NCI-designated Comprehensive Cancer Center, the Department of
730 Urology, Stanford University; NHLBI (P01HL10879709); NIAID (U19AI057229); and a
731 PICI Bedside to Bench grant. A.D.-G. thanks the Fundacion Alfonso Martin Escudero and
732 Ovarian Cancer Research Alliance for Mentored Investigator Award (MIG-2023-2-1015)
733 for his postdoctoral fellowships.

734 We wish to thank Dr Zach Bjornson for his design of new software in CellEngine to enable
735 part of our data analysis. We wish to thank Dr. Keith Shults and others for critical reading
736 of the manuscript and Professor Garry Nolan for the use of the CyTOF2 mass cytometer.

737

738 **Author contributions**

739 Conceptualization, W.J.F; J.D.B, J.S.S Methodology, V.D.G, Y.W-H, M.V, A.D.G,
740 Validation, J.S.B, I-G.F, Investigation, V.D.G, Y.W-H, A.D.G, Resources, V.D.G, Y.W-H,
741 M.V, A.D.G; Formal analysis, J.S.B, Z.R, A.M, A.L Data curation, J.S.B, Writing – Original
742 Draft, J.S.B; W.J.F Writing – Review & Editing, W.J.F, J.D.B, A.A, J.S.B I-G.F
743 Visualization, J.S.B, I-G.F, A.D.G, W.J.F, Funding Acquisition, W.J.F, A.A, J.D.B
744 Resources, M.E.V and C.K.B.; Supervision, W.J.F, J.D.B, A.A., Project administration,
745 W.J.F.

746 **Declaration of interests**

747 A.A. is a co-founder of Tango Therapeutics, Azkarra Therapeutics, Ovibio Corporation
748 and Kytarro, a member of the board of Cytomx and Cambridge Science Corporation, a
749 member of the scientific advisory board of Genentech, GLAdiator, Circle, Bluestar, Earli,
750 Ambagon, Phoenix Molecular Designs and Trial Library, a consultant for SPARC,
751 ProLynx, and GSK, receives grant or research support from SPARC and AstraZeneca,
752 and holds patents on the use of PARP inhibitors held jointly with AstraZeneca from which
753 he has benefited financially (and may do so in the future). J.D.B is a cofounder and
754 shareholder of Tailor, has had consulting and advisory roles in Astra Zeneca and Clovis
755 Oncology and has received honoraria from GSK and Astra Zeneca. W.J.F is currently
756 employed by Novartis and holds stock. W.J.F is an unpaid independent board member
757 for SurgeCare. She received an honorarium from GSK in 2022. All remaining authors
758 have no conflicts of interest to declare.

759

760 **Figure captions**

761 **Fig. 1: Characterization of the DNA damage response by CyTOF.**

762 **A.** Schema of experimental approach. Foundational experiments were performed using
763 TYK-nu and UWB1.289 HGSC cell lines. Validation was performed using three
764 spontaneously immortalized continuous HGSOC cell lines named CIOV1, CIOV2, and
765 CIOV3. **B.** Pathway map showing CyTOF antibody panel designed to measure proteins
766 participating in the carboplatin DNA damage response. Proteins marked in grey were not
767 measured because no suitable antibodies were available. “β-catenin” is non-phospho-β-
768 catenin **(Supp. Table 1** shows positive and negative controls for antibody validation).

769

770 **Fig. 2. Characterization of responses to carboplatin in the TYK-nu cell line.**

771 TYK-nu cells were treated with carboplatin, talazoparib, or both drugs and processed for
772 CyTOF analysis at the indicated times. **A.** Pie charts depict cell frequency distributions
773 across cell cycle phases. **B.** Biaxial plots displaying ^{195}Pt levels, which indicate
774 carboplatin uptake, plotted against c-PARP levels to differentiate apoptotic from non-
775 apoptotic cells to treatments over time. **C.** Box and whisker plot showing platinum uptake
776 in single intact cells and single isolated nuclei over time. CyTOF enabled characterization
777 of apoptotic populations at early times of drug treatments when cell frequencies were low
778 (~200 to 1000 cells). Boxes are colored by cell fate (apoptotic or non-apoptotic) and
779 compartment (whole cell (yellow) or nucleus (blue)). Notches are calculated to give a 95%
780 confidence interval comparing median values for ^{195}Pt uptake. **D.** Fold change in median
781 platinum levels comparing whole cells to nuclei for each timepoint and population.

782

783 **Fig. 3 Schema depicting unsupervised data analysis approach.**

784

785 **Fig. 4. Identification of DDR protein modules in TYK-nu cells.**

786 **A**. UMAP embedding generated with 29 DDR proteins, of single cell data from all
787 timepoints for 721,579 TYK-nu cells. Leiden cell clusters are overlaid on the UMAP and
788 colored. **B–E.** Partition-based graph abstraction plots show connectivity between Leiden
789 clusters. Plots are colored for cell fate, treatment, time, and cell cycle. Clusters are colored
790 with a pie-chart showing proportion of cells with different DDR features. **F and G.** DDR
791 protein modules discovered by non-negative matrix factorization (NMF). The matrix of
792 expression levels for 29 DDR proteins in 721,579 cells was decomposed into two

793 matrices. One discovered the most frequenctly co-occurring proteins in eight (number
794 user selected) DDR modules. The contribution of each protein within a specific module is
795 given by its z-score and this matrix is depicted on a hierarchically clustered heatmap. The
796 second matrix describes the activity of each module in an individual cell and is overlaid
797 on the UMAP. **H.** Box and whisker plots depict the activity of each module activity over
798 time.
799

800 **Fig. 5. Identification of DDR modules in UWB cells**

801 **A.** PAGA plot of Leiden clusters for UWB cells shows connectivity of clusters in high
802 dimensional space. Cluster nodes are colored based on an additional round of Leiden
803 clustering to identify highly interconnected clusters. **B–G.** PAGA plots colored for time,
804 treatment, cell fate, cell cycle phase, BRCA1-/BRCA1+ and pseudo time. **H.** DDR
805 modules identified by NMF as described in caption **5F**. The contribution of each protein
806 within a module is given by its Z-score depicted on a hierarchically clustered heatmap. **I.**
807 Module activity is depicted by the PAGA plot. Each Leiden cluster is colored with a pie-
808 chart to show the proportion of cells that recruit a specific module. Modules with less than
809 10% median activity in a cluster were excluded. **J.** Box and whisker plots depict the
810 activity of each module over time.
811

812 **Fig. 6. Characteristion of patient-derived ClOV1–3 cell lines.**

813 **A.** Violin plots depicting expression of epithelial, mesenchymal, stem cell, and HGSC
814 proteins. Key colored for cell line. **B.** Cell cycle distributions vary across cell lines in
815 response to treatments. **C.** Pie charts showing minimal apoptosis under the conditions

816 chosen. **D.** Box and whisker plots depicting 195-Pt uptake. Box colors correspond to cell
817 lines as in in **Fig. 6A**. Left to right within each cell line are treatment with carboplatin,
818 carboplatin + paclitaxel, and carbplatin +rucaparib. **E.** Violin plots depicting changes in
819 epithelial and mesenchymal states within each cell cycle phase in response to treatment.
820 EMT scores range from 0 to 1 with score of 1 indicating a purely epithelial phenotype and
821 a score of 0 indicating a purely mesenchymal phenotype and defined by levels of E-
822 cadherin and Vimentin.
823
824 **Fig. 7. Validation of TYK-nu NMF Module 6 in CIOV cell lines.**
825 In an independent experiment , CIOV1, 2 and 3 cell lines were treated with a carboplatin-
826 based regiment for 48 hr, and processed for CyTOF with the same DDR antibody panel.
827 **A.** Treatment journey showing patients whose tumors were responsive or resistant to
828 chemotherapy. Time for tumor acquisition is shown when samples were placed into 2D
829 cell culture to derive CIOVs 1, 2 and 3. **B.** Hierarchically clustered heatmap depicting
830 TYK-nu NMF Module usage. The values in the heatmap are pecentage increase in
831 module activity relative to DMSO control in CIOV cell lines under conditions shown.
832

References

1 Pilié, P. G., Tang, C., Mills, G. B. & Yap, T. A. State-of-the-art strategies for targeting the DNA damage response in cancer. *Nat Rev Clin Oncol* **16**, 81-104, doi:10.1038/s41571-018-0114-z (2019).

2 Maldonado, E. B., Parsons, S., Chen, E. Y., Haslam, A. & Prasad, V. Estimation of US patients with cancer who may respond to cytotoxic chemotherapy. *Future science OA* **6**, Fso600, doi:10.2144/fsoa-2020-0024 (2020).

3 Opzoomer, J. W., Sosnowska, D., Anstee, J. E., Spicer, J. F. & Arnold, J. N. Cytotoxic Chemotherapy as an Immune Stimulus: A Molecular Perspective on Turning Up the Immunological Heat on Cancer. *Frontiers in immunology* **10**, 1654, doi:10.3389/fimmu.2019.01654 (2019).

4 McGranahan, N. & Swanton, C. Clonal Heterogeneity and Tumor Evolution: Past, Present, and the Future. *Cell* **168**, 613-628, doi:10.1016/j.cell.2017.01.018 (2017).

5 Marusyk, A., Janiszewska, M. & Polyak, K. Intratumor Heterogeneity: The Rosetta Stone of Therapy Resistance. *Cancer Cell* **37**, 471-484, doi:10.1016/j.ccell.2020.03.007 (2020).

6 Bronder, D. *et al.* TP53 loss initiates chromosomal instability in fallopian tube epithelial cells. *Disease models & mechanisms* **14**, doi:10.1242/dmm.049001 (2021).

7 Cooke, S. L. & Brenton, J. D. Evolution of platinum resistance in high-grade serous ovarian cancer. *Lancet Oncol* **12**, 1169-1174, doi:10.1016/S1470-2045(11)70123-1 (2011).

8 Damia, G. & Broggini, M. Platinum Resistance in Ovarian Cancer: Role of DNA Repair. *Cancers* **11**, doi:10.3390/cancers11010119 (2019).

9 van Zyl, B., Tang, D. & Bowden, N. A. Biomarkers of platinum resistance in ovarian cancer: what can we use to improve treatment. *Endocrine-related cancer* **25**, R303-r318, doi:10.1530/erc-17-0336 (2018).

10 Matulonis, U. A. Management of newly diagnosed or recurrent ovarian cancer. *Clin Adv Hematol Oncol* **16**, 426-437 (2018).

11 Funingana, I. G. *et al.* Multiparameter single-cell proteomic technologies give new insights into the biology of ovarian tumors. *Seminars in immunopathology*, doi:10.1007/s00281-022-00979-9 (2023).

12 Morgan, R. D. *et al.* Objective responses to first-line neoadjuvant carboplatin-paclitaxel regimens for ovarian, fallopian tube, or primary peritoneal carcinoma (ICON8): post-hoc exploratory analysis of a randomised, phase 3 trial. *Lancet Oncol* **22**, 277-288, doi:10.1016/s1470-2045(20)30591-x (2021).

13 Richardson, D. L., Eskander, R. N. & O'Malley, D. M. Advances in Ovarian Cancer Care and Unmet Treatment Needs for Patients With Platinum Resistance: A Narrative Review. *JAMA Oncol* **9**, 851-859, doi:10.1001/jamaoncol.2023.0197 (2023).

14 Funingana, I. G., Reinius, M. A. V., Petrillo, A., Ang, J. E. & Brenton, J. D. Can integrative biomarker approaches improve prediction of platinum and PARP inhibitor response in ovarian cancer? *Seminars in cancer biology* **77**, 67-82, doi:10.1016/j.semcancer.2021.02.008 (2021).

15 Oliver, T. G. *et al.* Chronic cisplatin treatment promotes enhanced damage repair and tumor progression in a mouse model of lung cancer. *Genes Dev* **24**, 837-852, doi:10.1101/gad.1897010 (2010).

16 Miras, I., Estévez-García, P. & Muñoz-Galván, S. Clinical and molecular features of platinum resistance in ovarian cancer. *Crit Rev Oncol Hematol* **201**, 104434, doi:10.1016/j.critrevonc.2024.104434 (2024).

17 Burdett, N. L. *et al.* Multiomic analysis of homologous recombination-deficient end-stage high-grade serous ovarian cancer. *Nat Genet* **55**, 437-450, doi:10.1038/s41588-023-01320-2 (2023).

18 Swisher, E. M. *et al.* Secondary BRCA1 mutations in BRCA1-mutated ovarian carcinomas with platinum resistance. *Cancer Res* **68**, 2581-2586, doi:10.1158/0008-5472.can-08-0088 (2008).

19 Lord, C. J. & Ashworth, A. Mechanisms of resistance to therapies targeting BRCA-mutant cancers. *Nature medicine* **19**, 1381-1388, doi:10.1038/nm.3369 (2013).

20 Lin, K. K. *et al.* BRCA Reversion Mutations in Circulating Tumor DNA Predict Primary and Acquired Resistance to the PARP Inhibitor Rucaparib in High-Grade Ovarian Carcinoma. *Cancer discovery* **9**, 210-219, doi:10.1158/2159-8290.cd-18-0715 (2019).

21 Wang, Y. *et al.* The BRCA1-Δ11q Alternative Splice Isoform Bypasses Germline Mutations and Promotes Therapeutic Resistance to PARP Inhibition and Cisplatin. *Cancer Res* **76**, 2778-2790, doi:10.1158/0008-5472.can-16-0186 (2016).

22 Macintyre, G. *et al.* Copy number signatures and mutational processes in ovarian carcinoma. *Nat Genet* **50**, 1262-1270, doi:10.1038/s41588-018-0179-8 (2018).

23 Smith, P. *et al.* The copy number and mutational landscape of recurrent ovarian high-grade serous carcinoma. *Nature communications* **14**, 4387, doi:10.1038/s41467-023-39867-7 (2023).

24 Integrated genomic analyses of ovarian carcinoma. *Nature* **474**, 609-615, doi:10.1038/nature10166 (2011).

25 França, G. S. *et al.* Cellular adaptation to cancer therapy along a resistance continuum. *Nature* **631**, 876-883, doi:10.1038/s41586-024-07690-9 (2024).

26 Matsuoka, S. *et al.* ATM and ATR substrate analysis reveals extensive protein networks responsive to DNA damage. *Science* **316**, 1160-1166, doi:10.1126/science.1140321 (2007).

27 Olivieri, M. *et al.* A Genetic Map of the Response to DNA Damage in Human Cells. *Cell*, doi:10.1016/j.cell.2020.05.040 (2020).

28 Willis, N. A. *et al.* Identification of S-phase DNA damage-response targets in fission yeast reveals conservation of damage-response networks. *Proc Natl Acad Sci U S A* **113**, E3676-3685, doi:10.1073/pnas.1525620113 (2016).

29 Labrie, M., Brugge, J. S., Mills, G. B. & Zervantonakis, I. K. Therapy resistance: opportunities created by adaptive responses to targeted therapies in cancer. *Nat Rev Cancer* **22**, 323-339, doi:10.1038/s41568-022-00454-5 (2022).

30 Huang, R. & Zhou, P. K. DNA damage repair: historical perspectives, mechanistic pathways and clinical translation for targeted cancer therapy. *Signal transduction and targeted therapy* **6**, 254, doi:10.1038/s41392-021-00648-7 (2021).

31 Bendall, S. C., Nolan, G. P., Roederer, M. & Chattopadhyay, P. K. A deep profiler's guide to cytometry. *Trends in immunology* **33**, 323-332, doi:10.1016/j.it.2012.02.010 (2012).

32 Bjornson, Z. B., Nolan, G. P. & Fantl, W. J. Single-cell mass cytometry for analysis of immune system functional states. *Curr Opin Immunol* **25**, 484-494, doi:10.1016/j.coi.2013.07.004 (2013).

33 Spitzer, M. H. & Nolan, G. P. Mass Cytometry: Single Cells, Many Features. *Cell* **165**, 780-791, doi:10.1016/j.cell.2016.04.019 (2016).

34 Gonzalez, V. D., Huang, Y. W. & Fantl, W. J. Mass Cytometry for the Characterization of Individual Cell Types in Ovarian Solid Tumors. *Methods Mol Biol* **2424**, 59-94, doi:10.1007/978-1-0716-1956-8_4 (2022).

35 Fienberg, H. G., Simonds, E. F., Fantl, W. J., Nolan, G. P. & Bodenmiller, B. A platinum-based covalent viability reagent for single-cell mass cytometry. *Cytometry A* **81**, 467-475, doi:10.1002/cyto.a.22067 (2012).

36 Ornatsky, O. I. *et al.* Development of analytical methods for multiplex bio-assay with inductively coupled plasma mass spectrometry. *Journal of analytical atomic spectrometry* **23**, 463-469, doi:10.1039/b710510j (2008).

37 Behbehani, G. K., Bendall, S. C., Clutter, M. R., Fantl, W. J. & Nolan, G. P. Single-cell mass cytometry adapted to measurements of the cell cycle. *Cytometry A* **81**, 552-566, doi:10.1002/cyto.a.22075 (2012).

38 Domcke, S., Sinha, R., Levine, D. A., Sander, C. & Schultz, N. Evaluating cell lines as tumour models by comparison of genomic profiles. *Nature communications* **4**, 2126, doi:10.1038/ncomms3126 (2013).

39 Gonzalez, V. D. *et al.* Commonly Occurring Cell Subsets in High-Grade Serous Ovarian Tumors Identified by Single-Cell Mass Cytometry. *Cell reports* **22**, 1875-1888, doi:10.1016/j.celrep.2018.01.053 (2018).

40 Gonzalez, V. D. *et al.* High-grade serous ovarian tumor cells modulate NK cell function to create an immune-tolerant microenvironment. *Cell reports* **36**, 109632, doi:10.1016/j.celrep.2021.109632 (2021).

41 Vias, M. *et al.* Primary culture of high grade serous ovarian cancer cells, selection and derivation of three cell lines. *bioRxiv*, 2024.2008.2015.607946, doi:10.1101/2024.08.15.607946 (2024).

42 Yoshiya, N. *et al.* [Isolation of cisplatin-resistant subline from human ovarian cancer cell line and analysis of its cell-biological characteristics]. *Nihon Sanka Fujinka Gakkai zasshi* **41**, 7-14 (1989).

43 Coleman, R. L. *et al.* Veliparib with First-Line Chemotherapy and as Maintenance Therapy in Ovarian Cancer. *N Engl J Med* **381**, 2403-2415, doi:10.1056/NEJMoa1909707 (2019).

44 Dhawan, M. S. *et al.* Differential Toxicity in Patients with and without DNA Repair Mutations: Phase I Study of Carboplatin and Talazoparib in Advanced Solid Tumors. *Clin Cancer Res* **23**, 6400-6410, doi:10.1158/1078-0432.ccr-17-0703 (2017).

45 Olaussen, K. A. *et al.* PARP1 impact on DNA repair of platinum adducts: preclinical and clinical read-outs. *Lung cancer* **80**, 216-222, doi:10.1016/j.lungcan.2013.01.014 (2013).

46 Boussios, S. *et al.* Poly (ADP-Ribose) Polymerase Inhibitors: Talazoparib in Ovarian Cancer and Beyond. *Drugs in R&D* **20**, 55-73, doi:10.1007/s40268-020-00301-8 (2020).

47 Thomas, A., Murai, J. & Pommier, Y. The evolving landscape of predictive biomarkers of response to PARP inhibitors. *J Clin Invest* **128**, 1727-1730, doi:10.1172/JCI120388 (2018).

48 Murai, J. *et al.* Stereospecific PARP Trapping by BMN 673 and Comparison with Olaparib and Rucaparib. *Mol Cancer Ther* **13**, 433-443, doi:10.1158/1535-7163.MCT-13-0803 (2014).

49 Molinari, M. Cell cycle checkpoints and their inactivation in human cancer. *Cell proliferation* **33**, 261-274, doi:10.1046/j.1365-2184.2000.00191.x (2000).

50 Saleh, T. *et al.* Therapy-Induced Senescence: An "Old" Friend Becomes the Enemy. *Cancers* **12**, doi:10.3390/cancers12040822 (2020).

51 Chang, Q. *et al.* Single-cell measurement of the uptake, intratumoral distribution and cell cycle effects of cisplatin using mass cytometry. *Int J Cancer* **136**, 1202-1209, doi:10.1002/ijc.29074 (2015).

52 Wenzel, A. T. *et al.* Single-cell characterization of step-wise acquisition of carboplatin resistance in ovarian cancer. *NPJ systems biology and applications* **8**, 20, doi:10.1038/s41540-022-00230-z (2022).

53 Lord, C. J. & Ashworth, A. PARP inhibitors: Synthetic lethality in the clinic. *Science* **355**, 1152-1158, doi:10.1126/science.aam7344 (2017).

54 Ihnen, M. *et al.* Therapeutic potential of the poly(ADP-ribose) polymerase inhibitor rucaparib for the treatment of sporadic human ovarian cancer. *Mol Cancer Ther* **12**, 1002-1015, doi:10.1158/1535-7163.mct-12-0813 (2013).

55 Novohradsky, V., Zajac, J., Vrana, O., Kasparkova, J. & Brabec, V. Simultaneous delivery of olaparib and carboplatin in PEGylated liposomes imparts this drug combination hypersensitivity and selectivity for breast tumor cells. *Oncotarget* **9**, 28456-28473, doi:10.18632/oncotarget.25466 (2018).

56 Kelland, L. The resurgence of platinum-based cancer chemotherapy. *Nat Rev Cancer* **7**, 573-584, doi:10.1038/nrc2167 (2007).

57 Traag, V. A., Waltman, L. & van Eck, N. J. From Louvain to Leiden: guaranteeing well-connected communities. *Scientific reports* **9**, 5233, doi:10.1038/s41598-019-41695-z (2019).

58 Wolf, F. A. *et al.* PAGA: graph abstraction reconciles clustering with trajectory inference through a topology preserving map of single cells. *Genome Biol* **20**, 59, doi:10.1186/s13059-019-1663-x (2019).

59 Kotliar, D. *et al.* Identifying gene expression programs of cell-type identity and cellular activity with single-cell RNA-Seq. *eLife* **8**, doi:10.7554/eLife.43803 (2019).

60 Serrano, M. A. *et al.* DNA-PK, ATM and ATR collaboratively regulate p53-RPA interaction to facilitate homologous recombination DNA repair. *Oncogene* **32**, 2452-2462, doi:10.1038/onc.2012.257 (2013).

61 DelloRusso, C. *et al.* Functional characterization of a novel BRCA1-null ovarian cancer cell line in response to ionizing radiation. *Mol Cancer Res* **5**, 35-45, doi:10.1158/1541-7786.mcr-06-0234 (2007).

62 Shen, Y. T., Evans, J. C., Zafarana, G., Allen, C. & Piquette-Miller, M. BRCA Status Does Not Predict Synergism of a Carboplatin and Olaparib Combination in High-Grade Serous Ovarian Cancer Cell Lines. *Molecular Pharmaceutics* **15**, 2742-2753, doi:10.1021/acs.molpharmaceut.8b00246 (2018).

63 Masuda, T., Xu, X., Dimitriadis, E. K., Lahusen, T. & Deng, C. X. "DNA Binding Region" of BRCA1 Affects Genetic Stability through modulating the Intra-S-Phase Checkpoint. *International journal of biological sciences* **12**, 133-143, doi:10.7150/ijbs.14242 (2016).

64 Haghverdi, L., Buttner, M., Wolf, F. A., Buettner, F. & Theis, F. J. Diffusion pseudotime robustly reconstructs lineage branching. *Nat Methods* **13**, 845-848, doi:10.1038/nmeth.3971 (2016).

65 Shibue, T. & Weinberg, R. A. EMT, CSCs, and drug resistance: the mechanistic link and clinical implications. *Nat Rev Clin Oncol* **14**, 611-629, doi:10.1038/nrclinonc.2017.44 (2017).

66 Brenton, J. D. *et al.* Primary culture of high grade serous ovarian cancer cells, selection and derivation of three cell lines. *bioRxiv*, 2024.2008.2015.607946, doi:10.1101/2024.08.15.607946 (2024).

67 Chaffer, C. L., San Juan, B. P., Lim, E. & Weinberg, R. A. EMT, cell plasticity and metastasis. *Cancer Metastasis Rev* **35**, 645-654, doi:10.1007/s10555-016-9648-7 (2016).

68 Sun, X. & Kaufman, P. D. Ki-67: more than a proliferation marker. *Chromosoma* **127**, 175-186, doi:10.1007/s00412-018-0659-8 (2018).

69 Willems, E. *et al.* The functional diversity of Aurora kinases: a comprehensive review. *Cell division* **13**, 7, doi:10.1186/s13008-018-0040-6 (2018).

70 Janssens, S. & Tschopp, J. Signals from within: the DNA-damage-induced NF-kappaB response. *Cell Death Differ* **13**, 773-784, doi:10.1038/sj.cdd.4401843 (2006).

71 Prasetyanti, P. R. & Medema, J. P. Intra-tumor heterogeneity from a cancer stem cell perspective. *Molecular cancer* **16**, 41, doi:10.1186/s12943-017-0600-4 (2017).

72 Reyes-González, J. M. & Vivas-Mejía, P. E. c-MYC and Epithelial Ovarian Cancer. *Frontiers in oncology* **11**, 601512, doi:10.3389/fonc.2021.601512 (2021).

73 Polo, S. E. & Jackson, S. P. Dynamics of DNA damage response proteins at DNA breaks: a focus on protein modifications. *Genes Dev* **25**, 409-433, doi:10.1101/gad.2021311 (2011).

74 Kafri, P. *et al.* Quantifying β-catenin subcellular dynamics and cyclin D1 mRNA transcription during Wnt signaling in single living cells. *eLife* **5**, doi:10.7554/eLife.16748 (2016).

75 Marine, J. C., Dawson, S. J. & Dawson, M. A. Non-genetic mechanisms of therapeutic resistance in cancer. *Nat Rev Cancer*, doi:10.1038/s41568-020-00302-4 (2020).

76 Bartek, J. & Lukas, J. DNA damage checkpoints: from initiation to recovery or adaptation. *Current opinion in cell biology* **19**, 238-245, doi:10.1016/j.ceb.2007.02.009 (2007).

77 Brown, J. S., O'Carrigan, B., Jackson, S. P. & Yap, T. A. Targeting DNA Repair in Cancer: Beyond PARP Inhibitors. *Cancer discovery* **7**, 20-37, doi:10.1158/2159-8290.CD-16-0860 (2017).

78 Han, G. *et al.* Atomic mass tag of bismuth-209 for increasing the immunoassay multiplexing capacity of mass cytometry. *Cytometry A* **91**, 1150-1163, doi:10.1002/cyto.a.23283 (2017).

79 Behbehani, G. K. *et al.* Transient partial permeabilization with saponin enables cellular barcoding prior to surface marker staining. *Cytometry A* **85**, 1011-1019, doi:10.1002/cyto.a.22573 (2014).

80 Zunder, E. R. *et al.* Palladium-based mass tag cell barcoding with a doublet-filtering scheme and single-cell deconvolution algorithm. *Nature protocols* **10**, 316-333, doi:10.1038/nprot.2015.020 (2015).

81 Finck, R. *et al.* Normalization of mass cytometry data with bead standards. *Cytometry A*, doi:10.1002/cyto.a.22271 (2013).

82 Wolf, F. A., Angerer, P. & Theis, F. J. SCANPY: large-scale single-cell gene expression data analysis. *Genome Biol* **19**, 15, doi:10.1186/s13059-017-1382-0 (2018).

833 **Fig. 1**

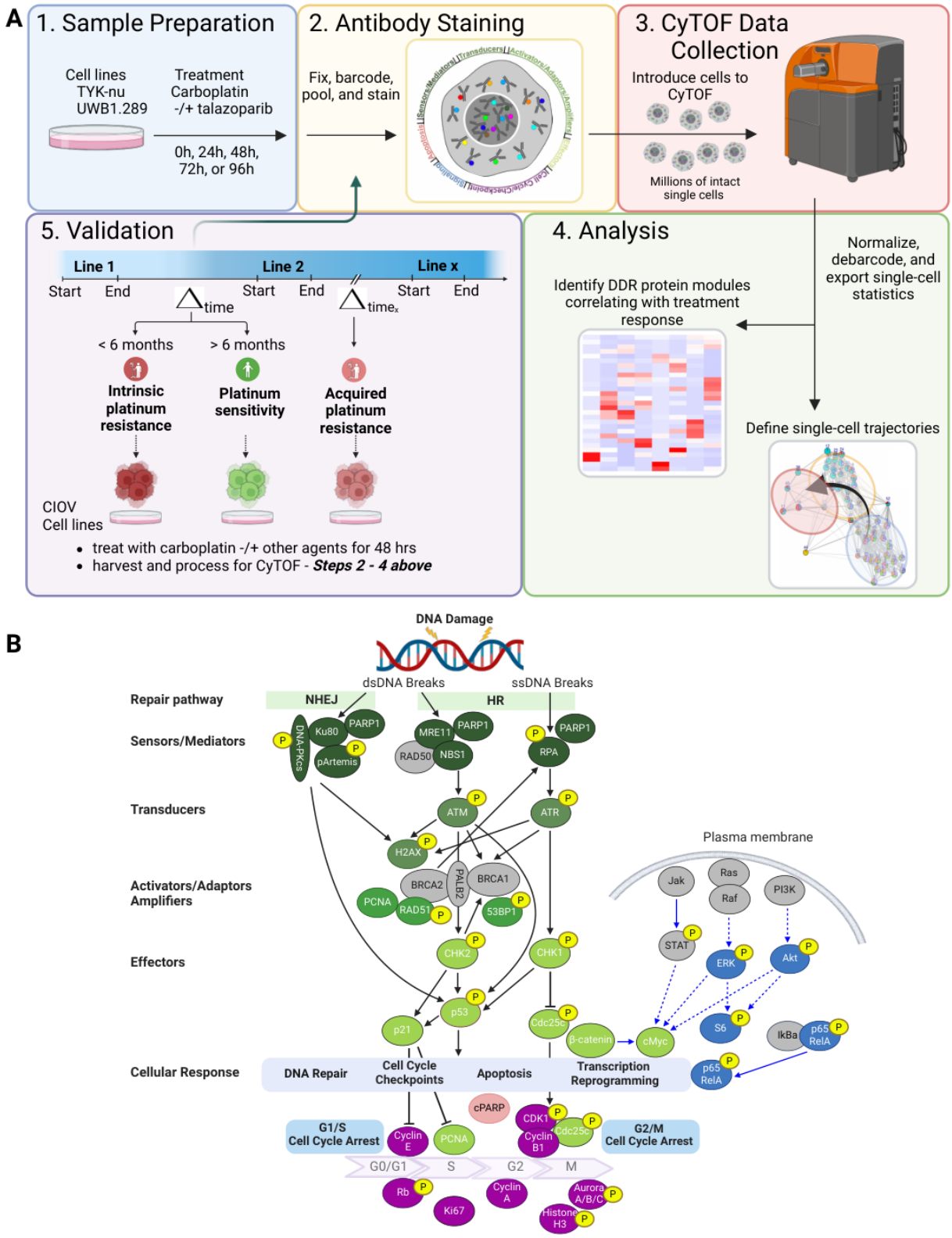
A
1. Sample Preparation
Cell lines
TYK-nu
UWB1.289
Treatment
Carboplatin
-/+ talazoparib
0h, 24h, 48h, 72h, or 96h
2. Antibody Staining
Fix, barcode, pool, and stain
3. CyTOF Data Collection
Introduce cells to CyTOF
Millions of intact single cells
4. Analysis
Normalize, debarcode, and export single-cell statistics
Identify DDR protein modules correlating with treatment response
Define single-cell trajectories
5. Validation
Line 1
Line 2
Line x
Start
End
time
time$_x$
< 6 months
> 6 months
Intrinsic platinum resistance
Platinum sensitivity
Acquired platinum resistance
CIOV Cell lines
treat with carboplatin -/+ other agents for 48 hrs
harvest and process for CyTOF - Steps 2 - 4 above
B
DNA Damage
dsDNA Breaks
ssDNA Breaks
Repair pathway
NHEJ
HR
Sensors/Mediators
Ku80
PARP1
DNA-PKcs
pArtemis
MRE11
RAD50
NBS1
RPA
Transducers
ATM
ATR
H2AX
Activators/Adaptors Amplifiers
BRCA2
PALB2
BRCA1
PCNA
RAD51
53BP1
Effectors
CHK2
CHK1
p53
p21
Cdc25c
β-catenin
cMyc
Plasma membrane
Jak
Ras
Raf
PI3K
STAT
ERK
Akt
S6
IkBa
p65 RelA
Cellular Response
DNA Repair
Cell Cycle Checkpoints
Apoptosis
Transcription Reprogramming
cPARP
G1/S Cell Cycle Arrest
Cyclin E
PCNA
CDK1
Cyclin B1
G2/M Cell Cycle Arrest
G0/G1
S
G2
M
Rb
Ki67
Cyclin A
Aurora A/B/C
Histone H3

834 **Fig. 2**

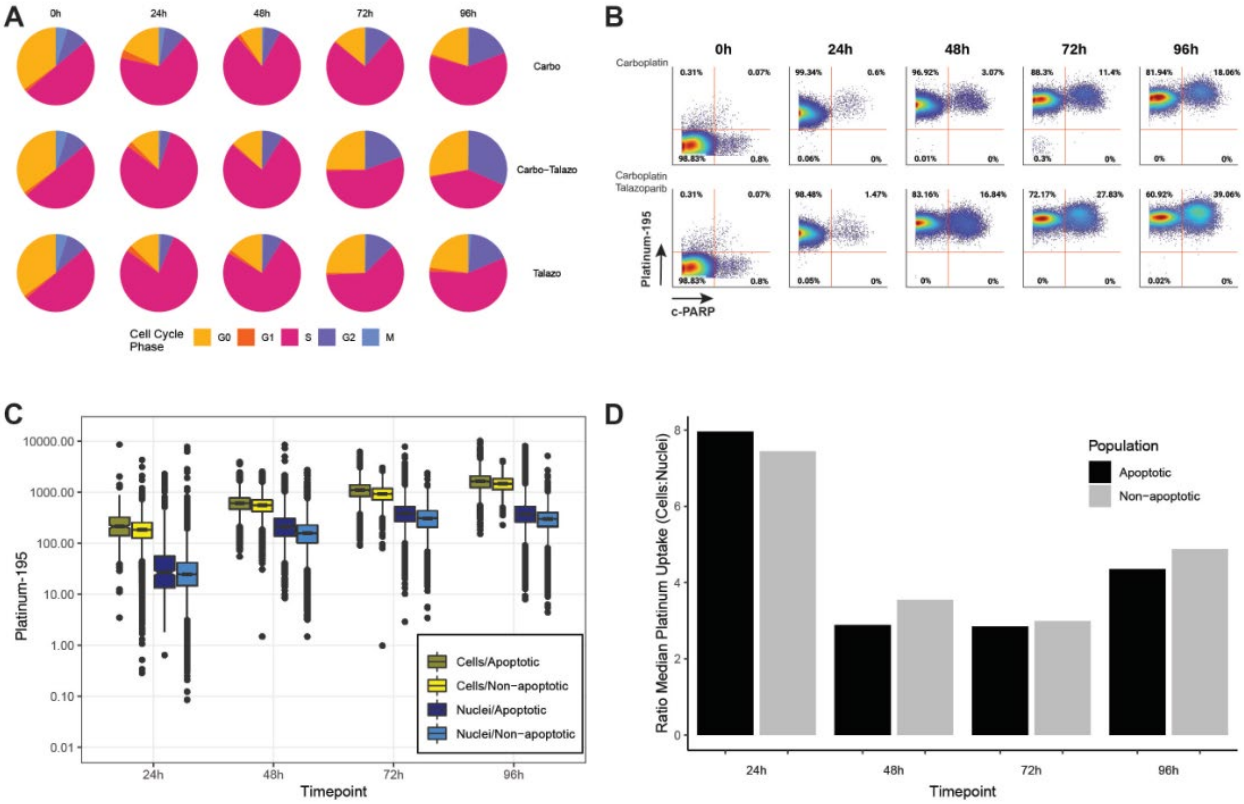
A
0h
24h
48h
72h
96h
Carbo
Carbo−Talazo
Talazo
Cell Cycle Phase
G0
G1
S
G2
M
B
0h
24h
48h
72h
96h
Carboplatin
Carboplatin Talazoparib
Platinum-195
c-PARP
C
Platinum-195
Timepoint
24h
48h
72h
96h
Cells/Apoptotic
Cells/Non−apoptotic
Nuclei/Apoptotic
Nuclei/Non−apoptotic
D
Ratio Median Platinum Uptake (Cells:Nuclei)
Population
Apoptotic
Non−apoptotic
Timepoint
24h
48h
72h
96h

835 **Fig. 3**

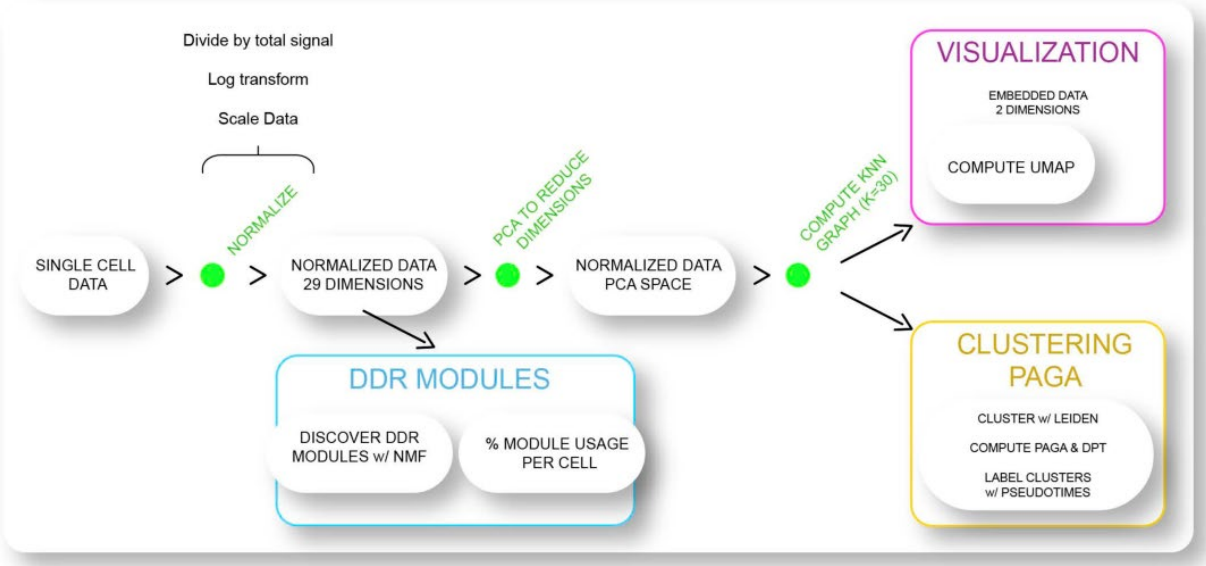
Divide by total signal
Log transform
Scale Data
NORMALIZE
SINGLE CELL DATA
NORMALIZED DATA 29 DIMENSIONS
PCA TO REDUCE DIMENSIONS
NORMALIZED DATA PCA SPACE
COMPUTE KNN GRAPH (K=30)
VISUALIZATION
EMBEDDED DATA 2 DIMENSIONS
COMPUTE UMAP
DDR MODULES
DISCOVER DDR MODULES w/ NMF
% MODULE USAGE PER CELL
CLUSTERING PAGA
CLUSTER w/ LEIDEN
COMPUTE PAGA & DPT
LABEL CLUSTERS w/ PSEUDOTIMES

836 **Fig. 4**

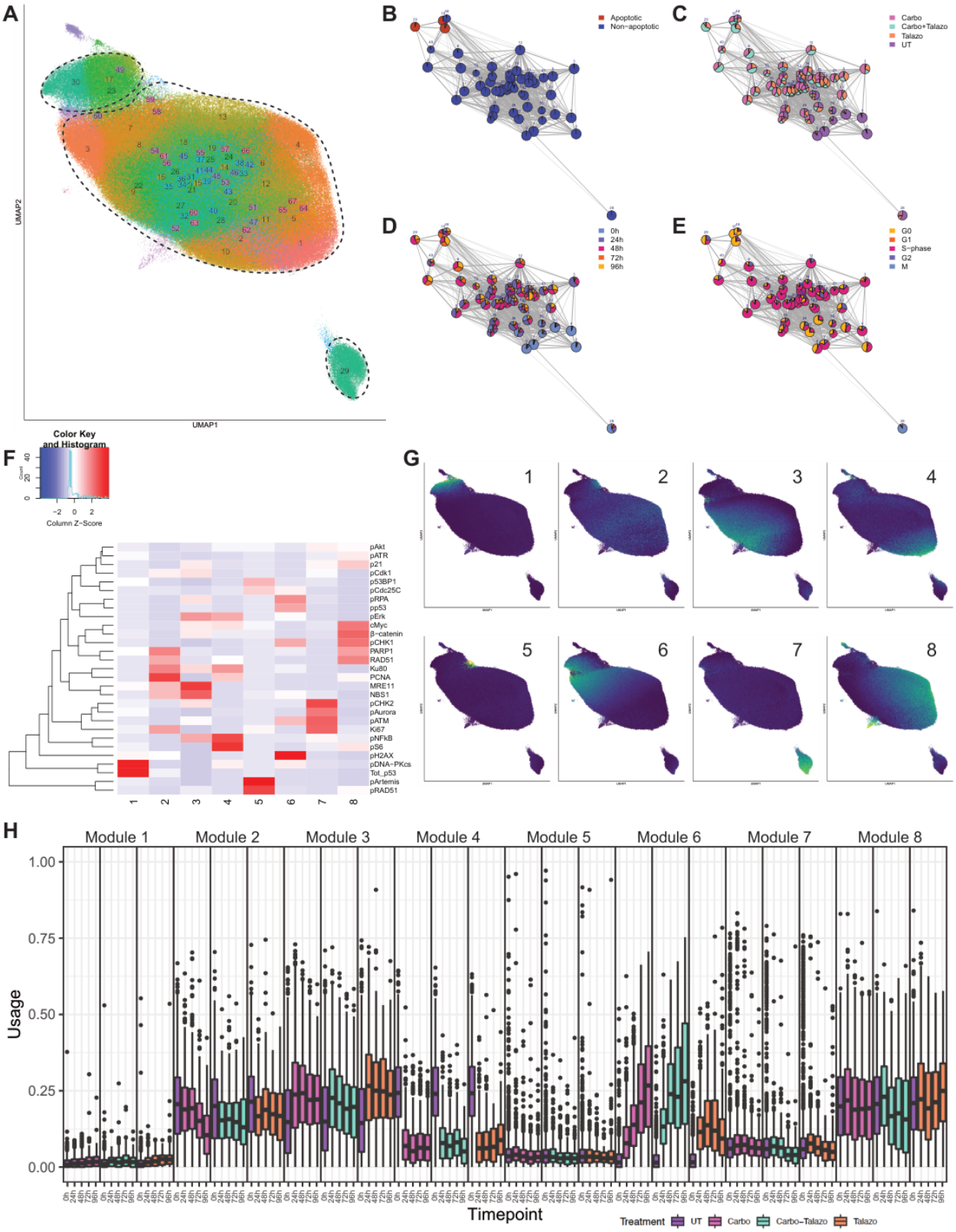
A
UMAP1
UMAP2
B
Apoptotic
Non-apoptotic
C
Carbo
Carbo+Talazo
Talazo
UT
D
0h
24h
48h
72h
96h
E
G0
G1
S-phase
G2
M
F
Color Key and Histogram
Count
Column Z-Score
pAkt
pATR
p21
pCdk1
p53BP1
pCdc25C
pRPA
pp53
pErk
cMyc
β-catenin
pCHK1
PARP1
RAD51
Ku80
PCNA
MRE11
NBS1
pCHK2
pAurora
pATM
Ki67
pNFkB
pS6
pH2AX
pDNA-PKcs
Tot_p53
pArtemis
pRAD51
G
H
Module 1
Module 2
Module 3
Module 4
Module 5
Module 6
Module 7
Module 8
Usage
Timepoint
Treatment
UT
Carbo
Carbo-Talazo
Talazo

837 **Fig. 5**

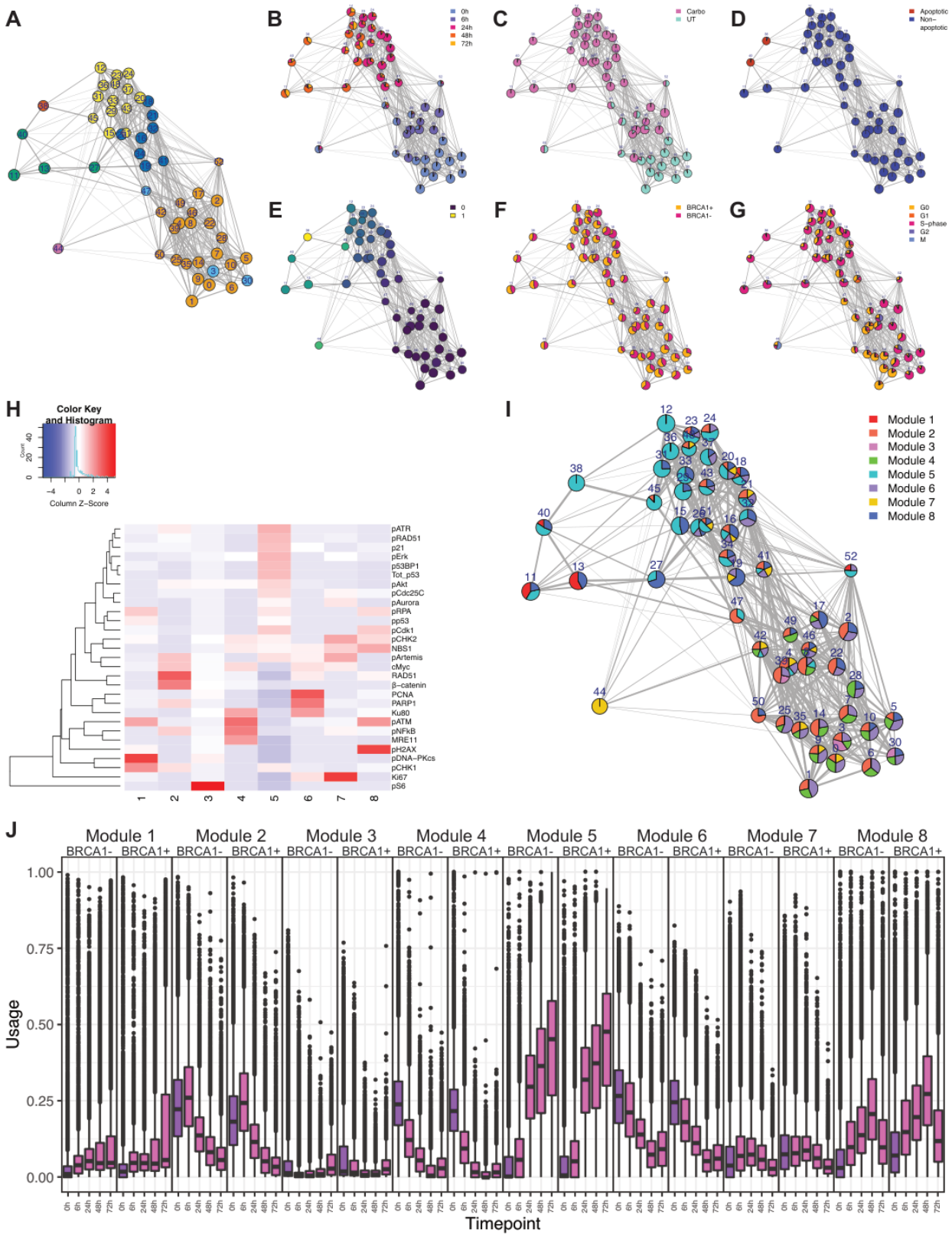
A
B
0h
6h
24h
48h
72h
C
Carbo
UT
D
Apoptotic
Non-apoptotic
E
0
1
F
BRCA1+
BRCA1-
G
G0
G1
S-phase
G2
M
H
Color Key and Histogram
Count
Column Z-Score
pATR
pRAD51
p21
pErk
p53BP1
Tot_p53
pAkt
pCdc25C
pAurora
pRPA
pp53
pCdk1
pCHK2
NBS1
pArtemis
cMyc
RAD51
β-catenin
PCNA
PARP1
Ku80
pATM
pNFkB
MRE11
pH2AX
pDNA-PKcs
pCHK1
Ki67
pS6
I
Module 1
Module 2
Module 3
Module 4
Module 5
Module 6
Module 7
Module 8
J
Module 1
Module 2
Module 3
Module 4
Module 5
Module 6
Module 7
Module 8
BRCA1-
BRCA1+
Usage
Timepoint

838 **Fig. 6**

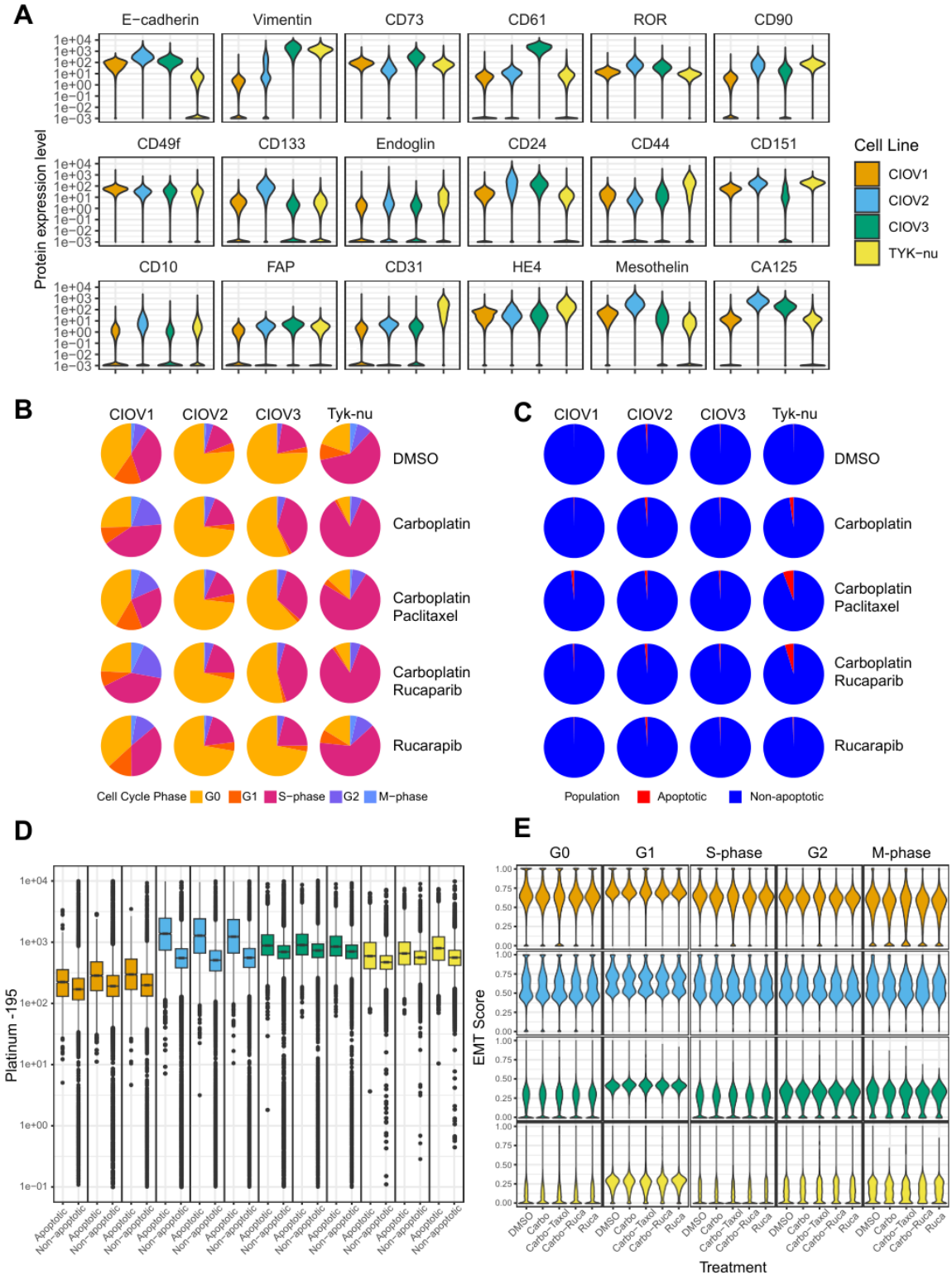
A
E−cadherin
Vimentin
CD73
CD61
ROR
CD90
CD49f
CD133
Endoglin
CD24
CD44
CD151
CD10
FAP
CD31
HE4
Mesothelin
CA125
Protein expression level
Cell Line
CIOV1
CIOV2
CIOV3
TYK−nu
B
CIOV1
CIOV2
CIOV3
Tyk-nu
DMSO
Carboplatin
Carboplatin Paclitaxel
Carboplatin Rucaparib
Rucarapib
Cell Cycle Phase G0 G1 S−phase G2 M−phase
C
Population Apoptotic Non-apoptotic
D
Platinum -195
Apoptotic
Non−apoptotic
E
G0
G1
S-phase
G2
M-phase
EMT Score
DMSO
Carbo
Carbo−Taxol
Carbo−Ruca
Ruca
Treatment

839 **Fig. 7**

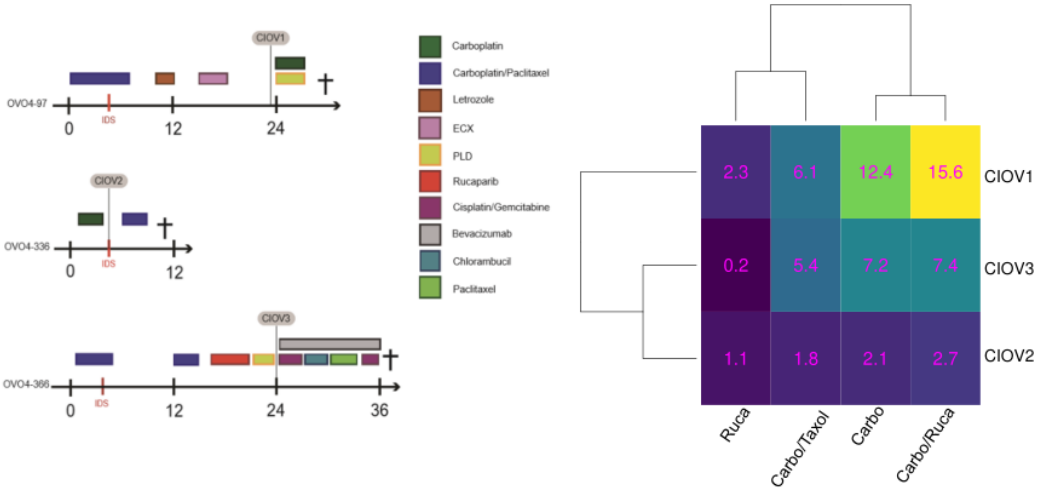
CIOV1
OVO4-97
IDS
0
12
24
CIOV2
OVO4-336
IDS
0
12
CIOV3
OVO4-366
IDS
0
12
24
36
Carboplatin
Carboplatin/Paclitaxel
Letrozole
ECX
PLD
Rucaparib
Cisplatin/Gemcitabine
Bevacizumab
Chlorambucil
Paclitaxel
2.3
6.1
12.4
15.6
CIOV1
0.2
5.4
7.2
7.4
CIOV3
1.1
1.8
2.1
2.7
CIOV2
Ruca
Carbo/Taxol
Carbo
Carbo/Ruca